Towards photocatalytic water splitting in homogeneous solutions using molecular metalloporphyrin photosensitizers and catalysts

Liu, C.

Citation

Liu, C. (2022, June 8). *Towards photocatalytic water splitting in homogeneous solutions using molecular metalloporphyrin photosensitizers and catalysts*. Retrieved from https://hdl.handle.net/1887/3307681

5

Summary, General discussion & Outlook

5.1 Summary of this thesis

Artificial photosynthesis (AP) is one of the scientific challenges that could help us achieving a global “carbon neutral” society. It will obviously remain an important research topic at least in the next 30 years. The general idea of AP is to use solar energy to either split water or reduce CO_2 into carbon fuels or organic products. Considering the argument that photovoltaic electricity generation followed by electrocatalysis inevitably causes energy losses, it is in principle more desirable to realize the AP reactions directly, preferably using earth-abundant elements. It is widely accepted that a photocatalytic system needs a minimum of three components: a photosensitizer (PS), a catalyst (Cat) and a sacrificial electron donor or acceptor (SE). In such a photocatalytic system, at least three electron-transfer steps can be identified: one between the SE and the excited PS (PS*), one between the photo-reduced or photo-oxidized PS and the Cat, and one between the Cat and its substrate. Since it is difficult to investigate the stability, activity, and catalytic mechanisms, of new molecular components in two photocatalytic processes running in parallel, half-reactions are often preferred. In addition, a well-defined homogeneous solution is simpler, hence better suited for the developments of molecular components, compared with heterogeneous or hybrid photocatalytic systems composed of self-assembled and/or solid-state components, in which the reacting species are sometimes difficult to identify. Therefore, all the research described in this thesis focused on developing improved molecular components for one of the two half reactions of water splitting, based on photocatalytic studies in purely homogeneous systems.

Although $[Ru(bpy)_3]^{2+}$ is based on a relatively rare metal it is also one of the best-known molecular photosensitizers capable of sensitizing both the light-driven oxygen-evolution reaction (OER) and the light-driven hydrogen-evolution reaction (HER). Thus, in this thesis it was used as standard PS for the development of new first-row transition metal catalysts for OER and HER. On the other hand, cobaloxime is a well-studied catalyst for photocatalytic HER, and it was selected as a standard hydrogen evolution catalyst (HEC) to develop new molecular photosensitizers based on earth-abundant elements. We combined both approaches to develop new catalysts and photosensitizers based on tetrasulfonated porphyrin ligands. Considering that for optimizing a photocatalytic system, a balance needs to be found between the driving force of electron transfer from the SE to the PS*, and that of electron transfer between the catalyst and the oxidized or reduced photosensitizer (PS^+ or $PS^–$), we systematically varied the electron richness of the porphyrin ligand by adding either electron-donating (8 methoxy or 8 methyl) or electron-withdrawing (8 or 16 fluorine) groups in ortho positions on the meso-phenyl rings (Figure 1.23 in **Chapter 1**).

In **Chapter 2**, the synthesis of a series of four tetra-anionic Ni(II)-porphyrin complexes using these ligands is described. These compounds were used as molecular catalysts for light-driven water oxidation in homogeneous neutral or acidic aqueous solutions. Electrochemical and kinetic studies demonstrated that more electron-withdrawing substituents increased the oxidation potentials of the Ni-porphyrin complexes, and controlled the oxygen-evolution rate in photocatalytic conditions. A balance had to be found between increasing these oxidation potentials, which provide a higher driving force for the catalytic OER itself, and keeping them low enough to make sure that the driving force for the electron transfer from the catalyst to the oxidized photosensitizer PS^+ is high enough. For example, when using $[Ru(bpy)_3]^{2+}$ as the photosensitizer and $S_2O_8^{2-}$ as the sacrificial electron acceptor, $[Ni\text{-}F16P]^{4-}$ was found to be too electron-poor, which blocked electron transfer between the nickel catalyst and the photo-oxidant $[Ru(bpy)_3]^{3+}$, thereby inactivating the photocatalytic system. The properties of $[Ni\text{-}F8P]^{4-}$ were found to be close to the optimum, resulting in excellent activity for the photocatalytic OER. Critically, these nickel porphyrin catalysts showed great stability in photocatalytic conditions, the TON of the photocatalytic system using $[Ni\text{-}F8P]^{4-}$ as catalyst was limited by the decomposition of the Ru-based photosensitizer. This work not only provides a rare example of homogeneous light-driven water oxidation catalysed by a Ni-based molecular catalyst in neutral to acidic aqueous solutions; it also provides new rules to design molecular catalysts for photocatalysis: the electron-density of the catalytic centre should be fine-tuned with appropriate substituents, to balance the driving forces of catalytic water oxidation vs. that of the electron transfer from the catalyst to PS^+.

In **Chapter 3** the synthesis is reported of analogous series of tetra-anionic Co(III)- and Zn(II)-porphyrin complexes, which were studied as molecular catalysts for homogeneous photocatalytic hydrogen generation in neutral and acid aqueous solutions. Although many cobalt-based molecular catalysts have been reported that can catalyze the HER, most of them have not been optimized for neutral aqueous solutions. This is unfortunate, because pH 7.0 is ideal for combining the water-oxidation and proton-reduction reaction into full water splitting. What is more, the catalytic mechanism of the HER in neutral conditions is not necessarily the same as in acidic solution, so that the strategy to design a catalyst optimized for neutral conditions may be different from one used to develop catalysts for acidic solutions. The photocatalytic activity and mechanism of the Co(III) and Zn(II) complexes were found to be strongly dependent on the presence of electron-withdrawing or electron-donating substituents on the porphyrin ring; they also were strongly dependent on the pH of the aqueous solution. In the series of zinc complexes the porphyrin ligands were found to be redox non-innocent, leading to significant photocatalytic HER for $[Zn\text{-}F16P]^{4-}$ in spite of the inability of the metal center to change its oxidation state. The electron-richest complex $[Co\text{-}OMeP]^{3-}$ had the highest driving force to reduce water in the series of cobalt porphyrin complexes, according to electrochemical analysis, but a higher photocatalytic activity was observed only at pH 4.1 that nearly vanished upon replacing the cobalt center by a zinc ion. At neutral pH, its activity was much lower than at low pH, and more interestingly much lower than that of the electron-poorest complex of the series, $[Co\text{-}F16P]^{3-}$. The activity of the latter compound in photocatalytic hydrogen evolution appeared to be comparatively low at pH 4.1, but excellent at neutral pH, resulting in comparable photocatalytic H_2 production quantum yields compared to that obtained with $[Co\text{-}OMeP]^{3-}$ at pH 4.1. According to our mechanistic studies the second reduction of $[Co\text{-}F16P]^{3-}$ by the photo-reduced species PS^{-}, which leads to hydrogen evolution, probably occurs via a pathway involving both the metal and the ligand; notably, it was partially retained when cobalt was replaced by zinc. Overall, this work represents a significant advance in our understanding of how to design a molecular hydrogen-evolution catalyst, because it indicated that it is not necessary to functionalize HER catalysts with electron-donating groups to enhance their catalytic activity, in particular in near-neutral aqueous conditions. Electron-withdrawing groups can also lead to excellent catalysts, although these follow a mechanism that differs from that obtained with electron-rich complexes. In photocatalytic systems aimed at driving full water splitting near pH 7.0, electron-poor cobalt-based hydrogen evolution catalyst (HEC) may be preferred, rather than the usually proposed electron-rich HEC which are only more active in acidic conditions.

Finally in **Chapter 4**, the synthesis of the analogous series of tetra-anionic Sn(IV)-porphyrin complexes is described. The photosensitizing properties of this new series of complexes, together with that of the Zn(II) analogues described in **Chapter 3**, were studied for the homogeneous photocatalytic HER in the presence of cobaloxime as standard HEC and TEOA as sacrificial electron donor in 1:1 pH 7.0 water/acetonitrile solutions. The photocatalytic activity obtained using these new PS molecules appeared to be highly depended on the electronic properties of the porphyrin ligand. Electrochemical studies and DFT calculations revealed that all photocatalytically active systems followed a reductive quenching pathway. For the Zn-porphyrin series, only the electron-poorest complex $[Zn\text{-}F16P]^{4-}$ led to significant hydrogen production, as characterized by a high activity (850 PTON after 20 h irradiation, 59 h^{-1} maximum PTOF) and a very high photostability: the complex remained active over 100 h under green light irradiation without observable decomposition. For the Sn-porphyrin series, the two electron-richest complexes $[\text{Sn-OMeP}]^{4-}$ and $[\text{Sn-MeP}]^{4-}$ showed significant sensitizing properties, but with a lower activity than $[\text{Zn-F16P}]^{4-}$ under the same conditions. Here as well the different electron-withdrawing and electron-donating ability of the substituents on the porphyrin ligand were found to control the redox properties and triplet excited state energies of the complex, which affected the thermodynamics and rates of electron transfer. This work is significant for the design and understanding of the mechanism of noble-metal-free molecular photosensitizers for hydrogen evolution. Indeed, it shows that a balance between the redox potentials of the ground-state PS and that of the excited state must be found, which are both controlled by the electron-donating or electron-withdrawing properties of the substituents.

5.2 General discussion

5.2.1 Strategy for the improvement of a homogeneous photocatalytic water-oxidation system via an oxidative quenching pathway

A homogeneous photocatalytic system for water splitting contains a photosensitizer (PS), and either a water-oxidation catalyst (WOC) and a sacrificial electron acceptor (EA) for water oxidation, or a hydrogen-evolution catalyst (HEC) and a sacrificial electron donor (ED) for hydrogen generation.[1] In theory, both oxidative and reductive quenching of the excited state PS* may take place for both photocatalytic OER and HER.[2] However, throughout the work reported in this thesis we only found an oxidative quenching pathway for the water-oxidation reaction and a reductive quenching pathway for hydrogen generation. In a simple but general approach, three types of electron-transfer steps can be distinguished between the three components of a photocatalytic system: the initial charge separation between PS* and either EA or ED (Step 1, in Figure 5.1); the electron transfer between PS^+ or PS^- and the catalyst (Step 2); and a series of catalytic electron-transfer steps between the oxidized or reduced catalyst and its substrate, sometimes coupled to proton transfer, to afford the products (Step 3).[3] According to the kinetic study described in **Chapter 2**, the oxygen-evolution rate using $[\text{Ni-F8P}]^{4-}$ as the WOC was limited by Step 2, i.e. electron transfer from the WOC to the PS^+. In **Chapter 3**, the hydrogen-generation rate using $[\text{Co-F16P}]^{3-}$ as catalyst at pH 7.0 appeared to be limited by Step 3, i.e., the catalytic proton reduction step. The hydrogen-evolution rate using $[\text{Co-OMeP}]^{3-}$ as catalyst at pH 4.1 appeared to be limited by the photon flux generating the excited photosensitizer PS*, which further affected the electron transfer Step 1, i.e., the generation of PS^{-}. Thus, the work described in this thesis clearly shows that in principle any of the three steps of a photocatalytic system can be the rate-determining step (RDS). Another important demonstration of this work is that an overall balance between these steps should be found in order to maximize the global rate of a photocatalytic system. In other words, there is no point in developing a faster catalyst if the rate-determining step (RDS) of the system is the intermolecular electron-transfer step of Step 2; it is not useful to look for a photosensitizer with a higher molar attenuation coefficient if the RDS is the catalytic step (Step 3); and it is naive to develop advanced supramolecular tools to increase local concentrations and speed up Step 2 if the RDS is photon absorption.[4]

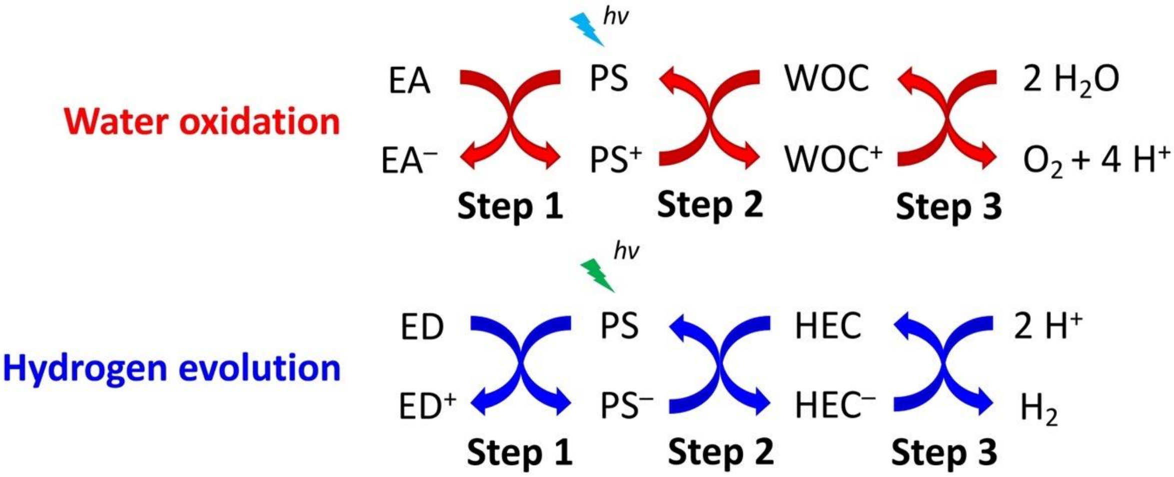

Figure 5.1 *Simplified mechanisms for homogeneous photocatalytic water oxidation and hydrogen evolution described in this thesis. EA: sacrificial electron acceptor; ED: sacrificial electron donor; PS: photosensitizer; WOC: water oxidation catalyst; HEC: hydrogen evolution catalyst; Step 1,2 or 3 are electron transfer steps.*

For a water-oxidation system in which PS* is oxidatively quenched, at a given pH the rate of Step 1 will be mostly controlled by the matching properties of EA and PS, that of Step 2 by the matching properties of PS and WOC, and the rate of Step 3 is only controlled by the properties of the WOC. The thermodynamics (i.e., the driving forces) of all three steps of a photocatalytic system are determinant to realize light-induced oxygen evolution. For example, a WOC with a higher overpotential, i.e., a higher potential at which the electrocatalysis starts to be significant (also known as onset potential), will have a higher driving force to obtain electrons from water. Similarly, a PS with a higher oxidation potential provides a higher driving force to oxidize the catalyst, resulting (in the normal region of Marcus' electron-transfer theory) in faster oxidation of the WOC to higher oxidation states, noted here symbolically WOC^+. Finally, an EA with a higher oxidation potential can offer more driving force to oxidize PS* to PS^+.

Thus, in theory, when the kinetics of the photocatalytic system is limited by Step 3, a WOC with a more positive oxidation potential will improve the overall photocatalytic oxygen evolution rate, which can be achieved by functionalizing the catalyst with electron-withdrawing substituents. When Step 2 is the RDS instead of Step 3, it is the PS that must be modified with electron-withdrawing groups if one wants to enhance the photocatalytic oxygen evolution. Finally, choosing an EA with a more positive reduction potential will lead to a faster oxygen generation only when Step 1 is the RDS of the system. However, for such modifications to lead to faster oxygen evolution important conditions are to be met: 1) the catalytic conditions should not be changed (for example, the pH or the concentrations); 2) modification of the molecule should not significantly change the photostability of the components, and 3) the catalytic mechanism of Step 3 should not change.

Still, it is worth noting that modifications on the electron density of one of the components in a photocatalytic system may change its kinetics appreciably. For example, modifying a PS with strong electron-withdrawing substituents on the one hand will make the PS^+ more prone to oxidize the WOC (Step 2), on the other hand it may make the triplet state oxidation potential more positive, which may make Step 1 slower. Similarly, a WOC with a higher overpotential may boost the rate of Step 3, but the driving force of Step 2 will be lower, thus leading to an overall oxygen evolution rate that may be lower or even zero. **Chapter 2** is a typical example of this effect: although the electron-poorest $[Ni\text{-}F16P]^{4-}$ has a very positive overpotential that could in principle lead to a very fast Step 3, but it was not active for photocatalytic oxygen evolution using $[Ru(bpy)_3]^{2+}$ as the PS because Step 2 was too slow, blocking the system. One should note that in such a case a photosensitizer with a higher oxidation potential than that of the $[Ru(bpy)_3]^{3+}/[Ru(bpy)_3]^{2+}$ couple may alleviate this problem and unravel the otherwise excellent electrocatalytic OER properties of this complex. Overall, one cannot emphasise enough that the global performances of a photocatalytic system is the result of the interplay between Step 1, Step 2, and Step 3. As a consequence, details of the photocatalytic mechanism need to be known before one is able to predict which influence substituting the PS or catalyst with electron-donating or electron-withdrawing groups will have on the photocatalytic properties of the system.

5.2.2 Strategy for the improvement of a homogeneous photocatalytic hydrogen evolution system via a reductive quenching pathway

At first sight, a very similar analysis can be made for photocatalytic hydrogen evolution in the case of reductive quenching. In **Chapter 3**, the cobalt porphyrin HEC with higher electron richness indeed made the photocatalytic system more active in acidic conditions: the electron-richest catalyst $[Co\text{-}OMeP]^{3-}$ led to better photocatalytic activity than $[Co\text{-}MeP]^{3-}$ at pH 4.1. On the other hand, the electron-poor $[Co\text{-}F8P]^{3-}$ led to faster photocatalytic H_2 production than $[Co\text{-}MeP]^{3-}$ (Figure 3.4). Although we did not do a full kinetic study for these two catalysts, we can hypothesize that the less negative onset potential of $[Co\text{-}MeP]^{3-}$, compared to all three other complexes of the series (Figure 3.3d), might explain its poor performance in photocatalytic conditions, as it may limit the rate of Step 3.

Overall, the fact that the influence of the electron richness of the HEC on photocatalytic HER is complicated, was best demonstrated by our pH-dependent studies. $[Co\text{-}OMeP]^{3-}$ has the highest overpotential η of the series, which according to our analysis leads to a fast Step 3 at pH 4.1, and as Step 2 is also fast, the hydrogen-evolution rate of the system was limited by the photon flux (Step 1). In contrast, the electron-poorest HEC $[Co\text{-}F16P]^{3-}$ gave a higher TON and TOF in photocatalytic conditions at pH 7.0, compared with that of $[Co\text{-}OMeP]^{3-}$, because the electron-withdrawing effect of 16 fluoro substituents changes the catalytic hydrogen generation mechanism of Step 3. Although these electron-withdrawing substituents give to $[Co\text{-}F16P]^{3-}$ unexpected high activity, according to our kinetic study, this photocatalytic system is still controlled by Step 3. We interpret this observation as a consequence on the one hand of the low H_2 generation overpotential η for this complex, which limits the rate of Step 3, and on the other hand of the strongly reducing properties of $[Ru(bpy)_3]^+$ that provide a high driving force for Step 2. Clearly, though many people would claim that electron-donating substituents are better for HEC, our work demonstrates that electron-withdrawing groups can also lead to surprisingly good HEC, which is one of the most striking findings in this thesis.

For the PS, introducing electron-donating groups generates a more negative reduction potential, which in principle provides more driving force to transfer electron from PS^- to the HEC. However, in **Chapter 4** we found that modifications of the electron density of the PS had to be performed carefully. Indeed, an electron-richer porphyrin ligand not only made the PS more difficult to be reduced in the ground state, but it also decreased the triplet excited energy of the PS* slightly, which made the reduction potential of the triplet state of the PS less positive. This kind of changes generated a lower driving force for the electron transfer of Step

1, which may block the photocatalytic system. For example, for the system based on [Zn-F8P]$^{4-}$ the electron transfer of Step 1 was not thermodynamically feasible, while in the system containing the electron-poor PS [Zn-F16P]$^{4-}$, Step 1 did occur. On the other hand, in the Sn-porphyrin series, [Sn-F8P]$^{4-}$ and [Sn-F16P]$^{4-}$ were found to be too electron-poor: they did not have a sufficiently negative reduction potential to provide enough driving force to drive Step 2. In this case, the introduction of electron-donating substituents, such as in [Sn-OMeP]$^{4-}$ or [Sn-MeP]$^{4-}$, led to a more negative reduction potential of these otherwise electron-poor PSs, which was more efficient for the overall photocatalytic scheme.

To sum up, the optimization of a homogeneous photocatalytic hydrogen evolution system characterized by a reductive quenching pathway can only be achieved by increasing the driving force and rate of the RDS. In particular, this effect can be obtained using a HEC with a more negative on-set potential, a PS modified with more electron-donating groups, or an ED with a more negative oxidation potential, when Step 3, 2, or 1, limits the catalytic system, respectively; alternatively, better light absorption properties could also contribute to faster Step 1. Like adding electron-withdrawing groups to a WOC for water oxidation, adding electron donating groups to PS or HEC should be done carefully, making sure that: 1) the photocatalytic conditions and the RDS do not change, 2) the modifications do not significantly change the photostability of the components of the system, and 3) the hydrogen evolution catalytic mechanism of the HEC (Step 3) does not change. Clearly, for [Co-F16P]$^{3-}$ at pH 7.0 the first and third condition were not met, and electron-withdrawing groups led to an enhancement of the photocatalytic H_2 evolution, compared to [Co-OMeP]$^{3-}$.

5.3 Outlook

In the word described in this thesis, different homogeneous photocatalytic systems were investigated in particular for photocatalytic water oxidation and hydrogen evolution. In order to achieve the target of artificial photosynthesis, efforts on photocatalytic CO_2 reduction reaction (CO_2RR) are still needed. Iron porphyrin complexes have been reported to perform the CO_2RR with high activity and selectivety.[5] It would be interesting to prepare the iron analogues of the nickel, cobalt, zinc, and tin porphyrin complexes reported in this thesis, and to study them as catalysts for the photocatalytic CO_2RR, to investigate the effects of the electron density of the catalyst on this reaction. We should mention that the analoguous series of copper(II) complexes was prepared during the work described in this thesis, and these were sent to different collaborators for evaluating their catalytic properties for the CO_2RR and for the dioxygen reduction reaction.

The homogeneous photocatalytic water described in **Chapter 2** was only studied using $[Ru(bpy)_3]^{2+}$ as the PS. Since this photosensitizer is notoriously unstable under the harsh conditions of the light-driven OER,[6] and since its oxidation potential in the ground state is only +1.26 V vs. NHE,[4] it would be interesting to develop a more robust photosensitizer that would be free of any noble metal and that would have a more positive oxidation potential in the ground state. Such a PS could be prepared for example using the electron-poor $[H_2\text{-F16P}]^{4-}$ ligand described in this thesis with a specifically chosen metal center that would provide enough driving force to oxidize a WOC having a high overpotential such as $[\text{Ni-F16P}]^{4-}$. For example, $[\text{Zn-F16P}]^{4-}$ and all 4 tin(IV)-porphyrin complexes described in **Chapter 4** have a higher oxidation potential in the ground state than $[Ru(bpy)_3]^{2+}$. They also have less energy in their excited state E(T), but the resulting excited state potentials $E_{PS*,ox}(PS^+/PS^*)$, which culminates at –0.01 V vs. NHE for $[\text{Sn-MeP}]^{4-}$, are still more negative than the potential necessary for reducing the $S_2O_8^{2-}$ anion (+0.6 V vs. NHE). Hence, all 5 molecules are, in theory, eligible for sensitizing the OER catalyzed by $[\text{Ni-F16P}]^{4-}$.

Last but not least, an overall photocatalytic water-splitting system may be established using the catalysts reported in **Chapter 2** and **Chapter 3**, and the photosensitizers described in **Chapter 4**. When this PhD work was completed, both half-reactions of water splitting (OER and HER) worked independently, in the presence of sacrificial electron acceptor and donor. In theory, both half-reactions might be bridged into a single water-splitting system provided that an electron relay (or a couple of electron relays) can be found that transports electrons (and protons) from the WOC to the HEC. Two systems are suggested in Figure 5.2. First, solid electrodes could be used to transport electrons (system A), while protons would be moved from one side of the system to the other via a proton-conducting membrane.[7] It is noteworthy that in such a photoelectrochemical system, a single PS might be used for both half-reactions if its photo-redox properties are sufficient to drive both the OER and the HER. This is a well-known advantage of $[Ru(bpy)_3]^{2+}$, but it still remains to be proven that the same property can be obtained with a more stable PS based on an earth-abundant metal. Second, the combination of tetrachlorobenzoquinone/tetrachlorobenzo–hydrosemiquinone (TCBQ/TCBQH) embedded in the lipid membrane of a negatively charged liposome, with Fe^{3+}/Fe^{2+} dissolved in the aqueous solution around the membrane, may be used (system B).[8] In such a negatively charged liposome-supported system, the protons would be transported together with the electron through the membrane by the hydrophobic hydrosemiquinone electron relay, as quinones are usually reduced by proton-coupled electron transfer. The PS on the HER side should be positively charged in order to stay close to the membrane and allow electron transfer to the quinone relay in the membrane. Commercially available $[Ru(bpy)_3]^{2+}$ or 5,10,15,20-tetrakis(4-N-methylpyridinium)porphyrin zinc(II) compounds are potential candidates for such photosensitizers. All in all, although the development of new molecular photosensitizers and catalysts is a great advance in the field of artificial photosynthesis, combining both half-reactions in a single photocatalytic system remains one of the greatest challenges of the photochemistry and supramolecular chemistry of the 21th century.

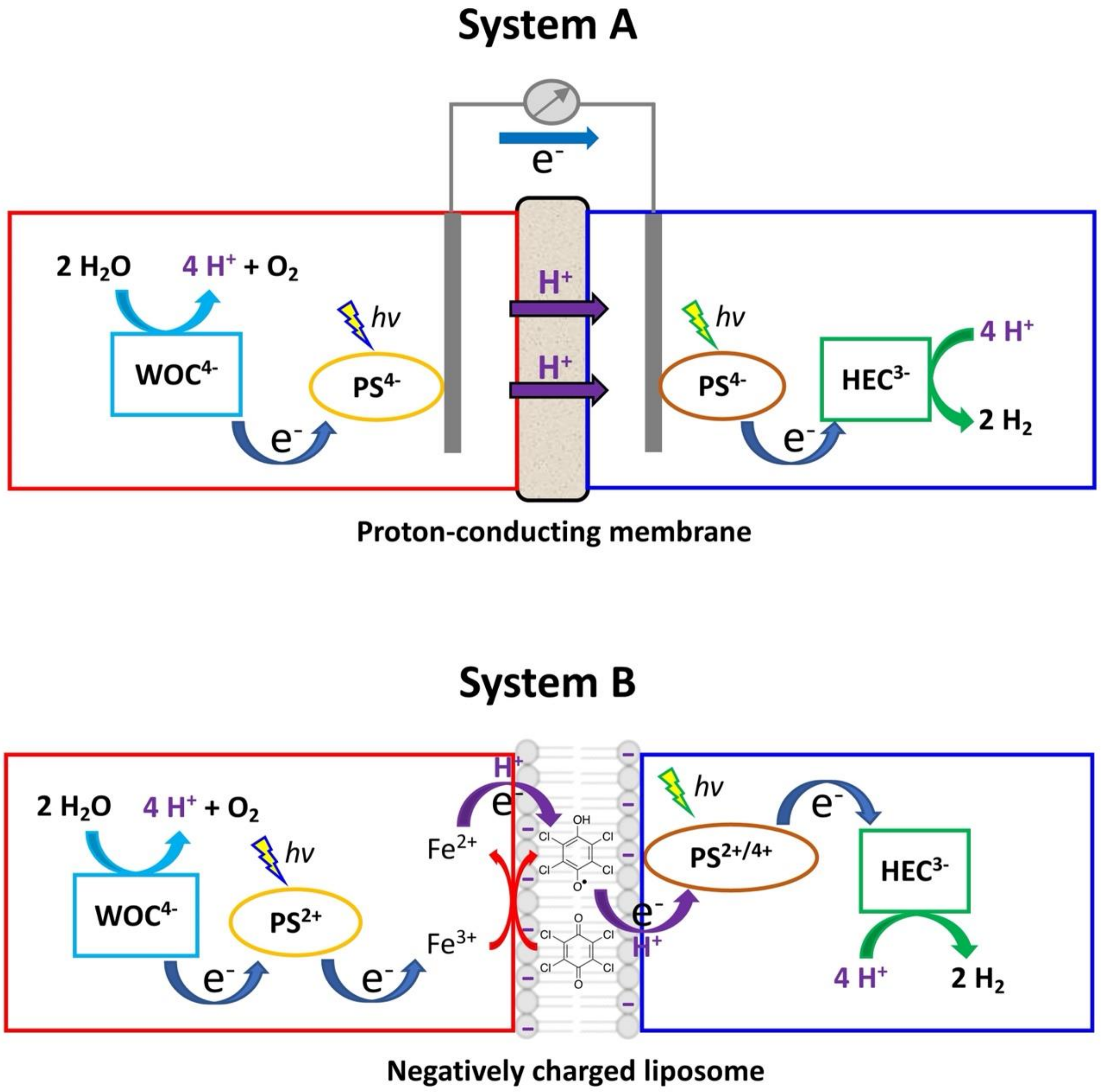

Figure 5.2 *Two general architectures for full photocatalytic water splitting. PS: photosensitizer; HEC: hydrogen evolution catalyst; WOC: water oxidation catalyst.*

5.4 References

[1] K. E. Dalle, J. Warnan, J. J. Leung, B. Reuillard, I. S. Karmel, E. Reisner, *Chem. Rev.* **2019**, *119*, 2752-2875.

[2] W. T. Eckenhoff, *Coord. Chem. Rev.* **2018**, *373*, 295-316.
[3] Y. J. Yuan, Z. T. Yu, D. Q. Chen, Z. G. Zou, *Chem. Soc. Rev.* **2017**, *46*, 603-631.
[4] C. Liu, D. van den Bos, B. den Hartog, D. van der Meij, A. Ramakrishnan, S. Bonnet, *Angew. Chem. Int. Ed.* **2021**, *60*, 13463-13469.
[5] H. Rao, L. C. Schmidt, J. Bonin, M. Robert, *Nature* **2017**, *548*, 74-77.
[6] U. S. Akhtar, E. L. Tae, Y. S. Chun, I. C. Hwang, K. B. Yoon, *ACS Catal.* **2016**, *6*, 8361-8369.
[7] M. D. Karkas, O. Verho, E. V. Johnston, B. Akermark, *Chem. Rev.* **2014**, *114*, 11863-12001.
[8] H. Hu, Z. Wang, L. Cao, L. Zeng, C. Zhang, W. Lin, C. Wang, *Nat. Chem.* **2021**, *13*, 358-366.

APPENDIX I: SUPPORTING INFORMATION FOR CHAPTER 2

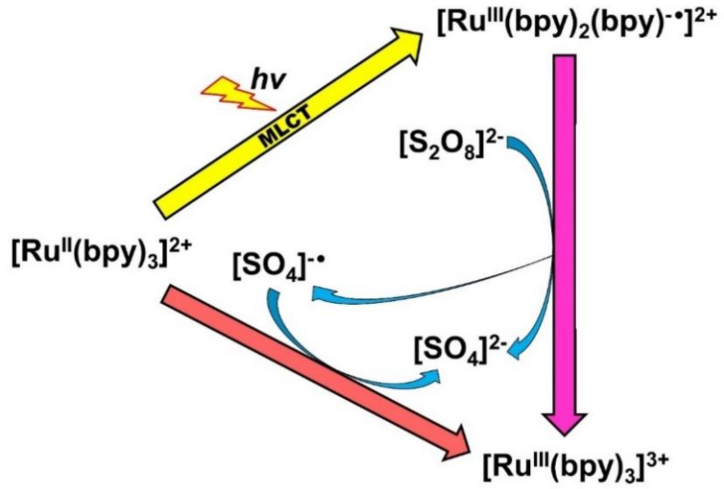

Figure AI.1 *Simplified mechanism of Step 1 of Figure 2.2 in [Ru(bpy)$_3$]$^{2+}$ coupled with [S$_2$O$_8$]$^{2-}$ system for molecular homogeneous photocatalytic water oxidation. MLCT: Metal-to-ligand charge transfer.*

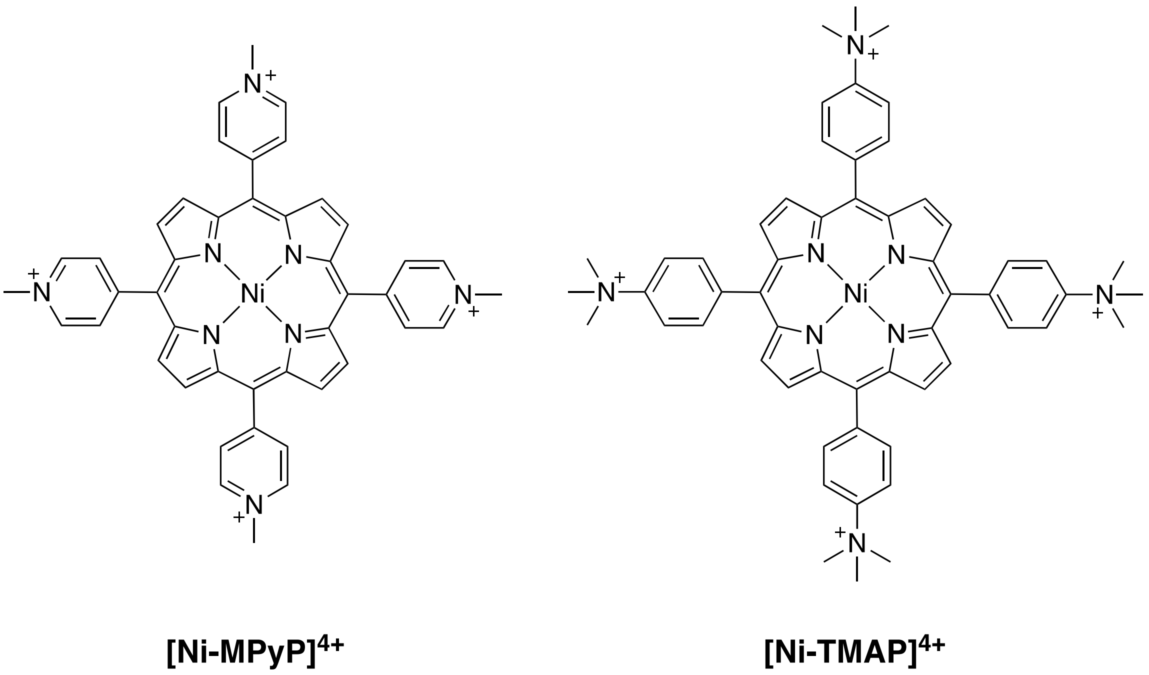

Figure AI.2 *Chemical structures of two positively charged water-soluble Ni(II)-porphyrin complexes as controls in this work, isolated as trifluoromethanesulfonate salts.*

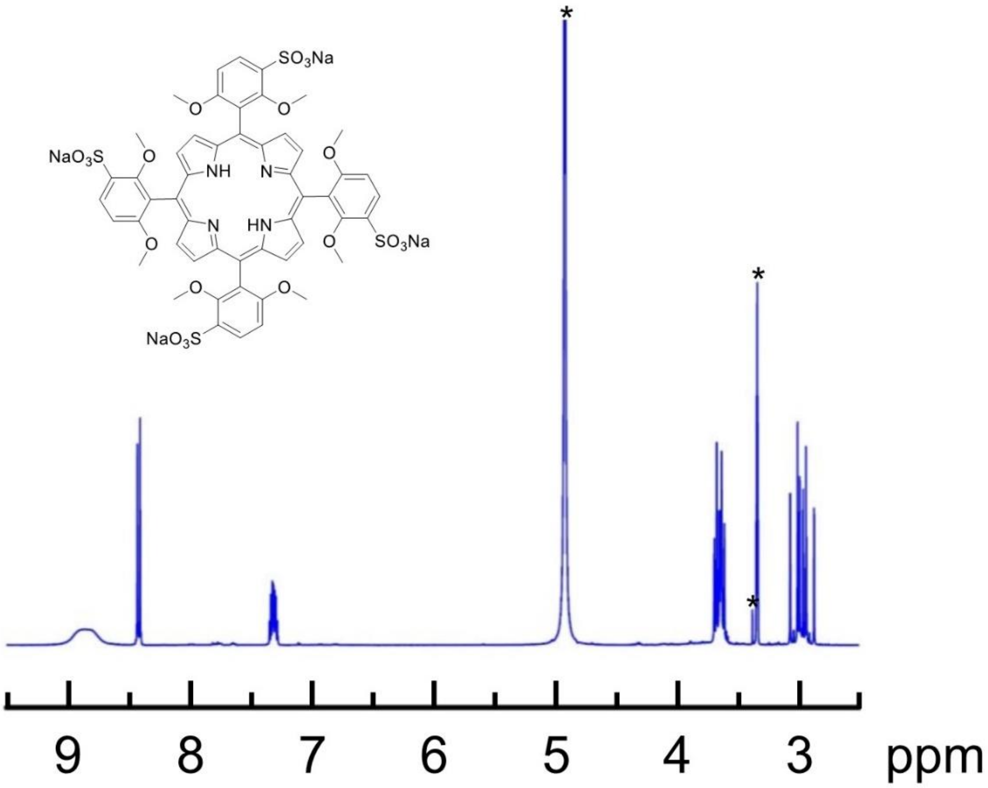

Figure AI.3 *^{1}H NMR of $Na_4[H_2\text{-OMeP}]$ in CD_3OD. * Methanol and water.*

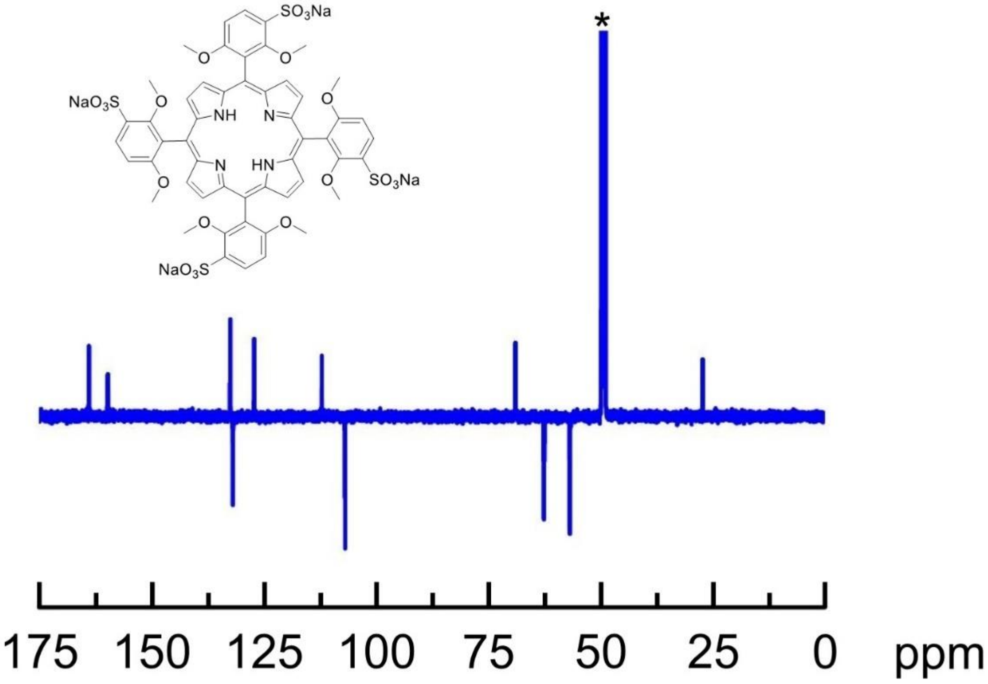

Figure AI.4 *^{13}C NMR of $Na_4[H_2\text{-OMeP}]$ in CD_3OD. * Methanol.*

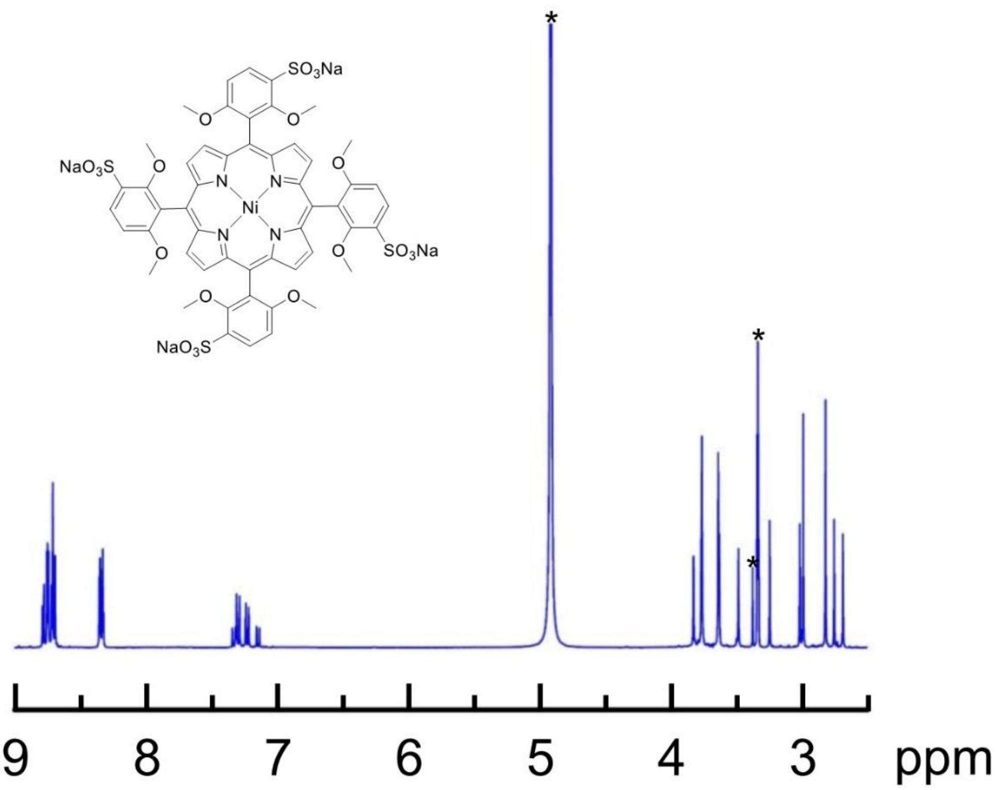

Figure AI.5 *^{1}H NMR of Na_4[Ni-OMeP] in CD_3OD. * Methanol and water.*

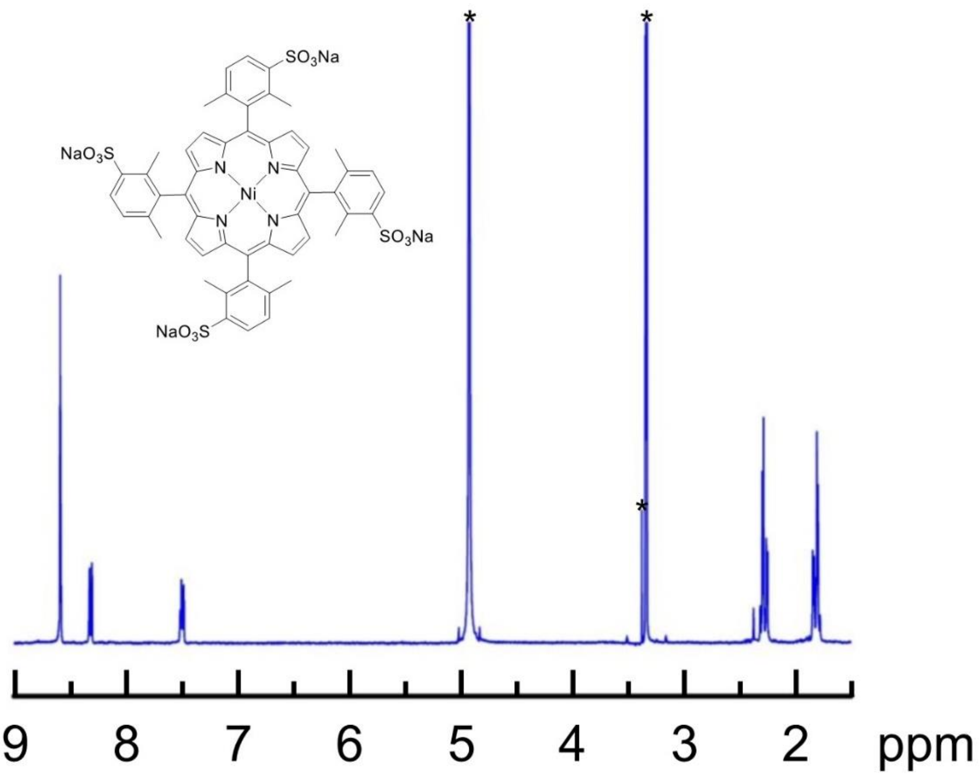

Figure AI.6 *^{1}H NMR of Na_4[Ni-MeP] in CD_3OD. * Methanol and water.*

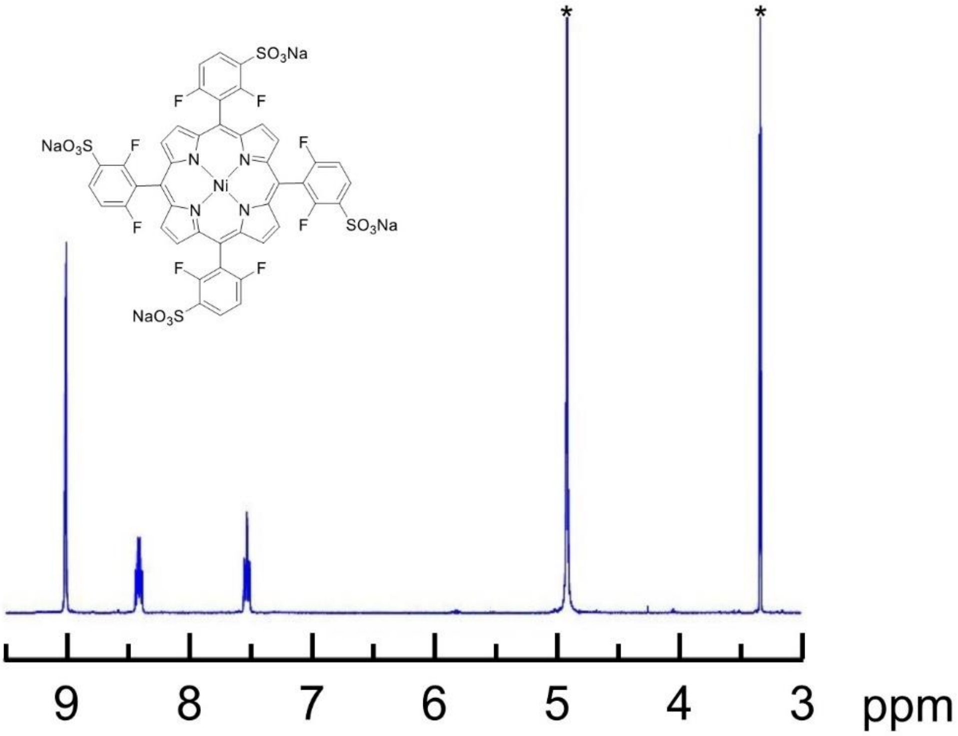

Figure AI.7 *^{1}H NMR of Na_4[Ni-F8P] in CD_3OD. * Methanol and water.*

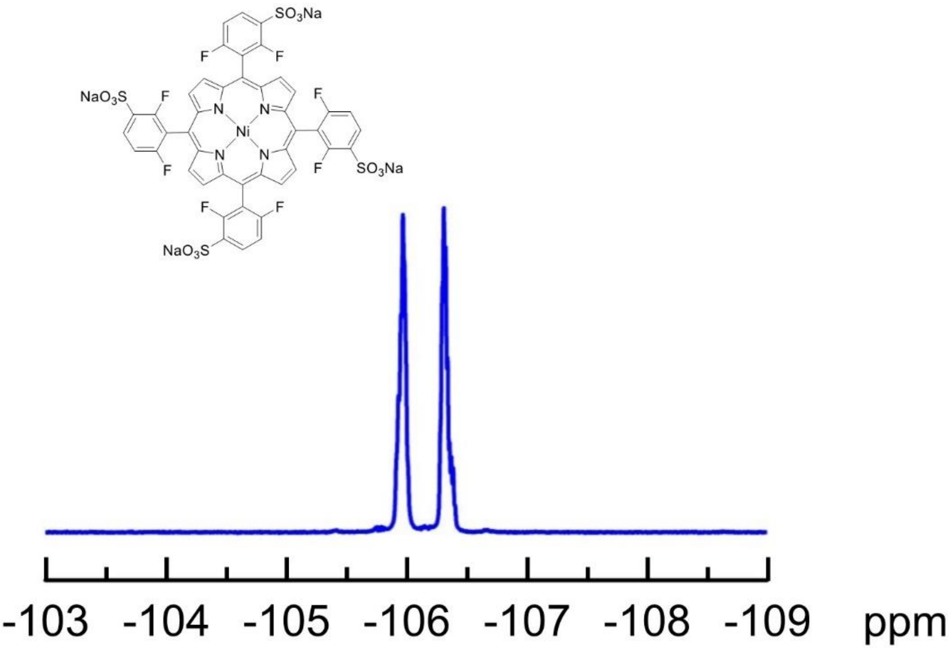

Figure AI.8 *^{19}F NMR of Na_4[Ni-F8P] in CD_3OD. * Methanol and water.*

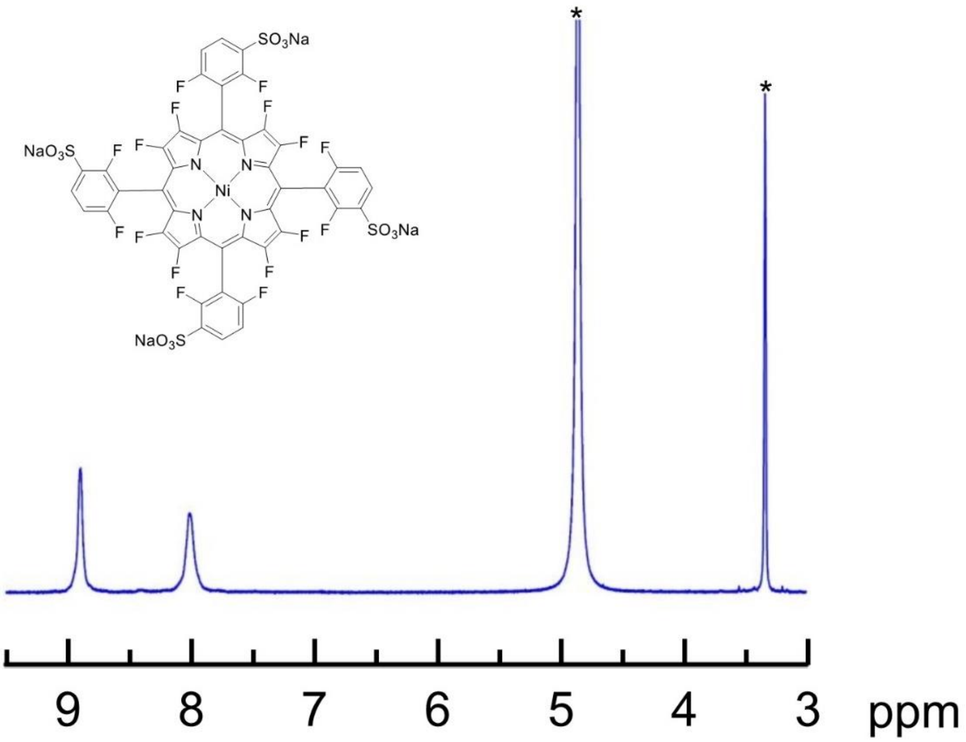

Figure AI.9 *^{1}H NMR of $Na_4[Ni\text{-}F16P]$ in CD_3OD. * Methanol and water.*

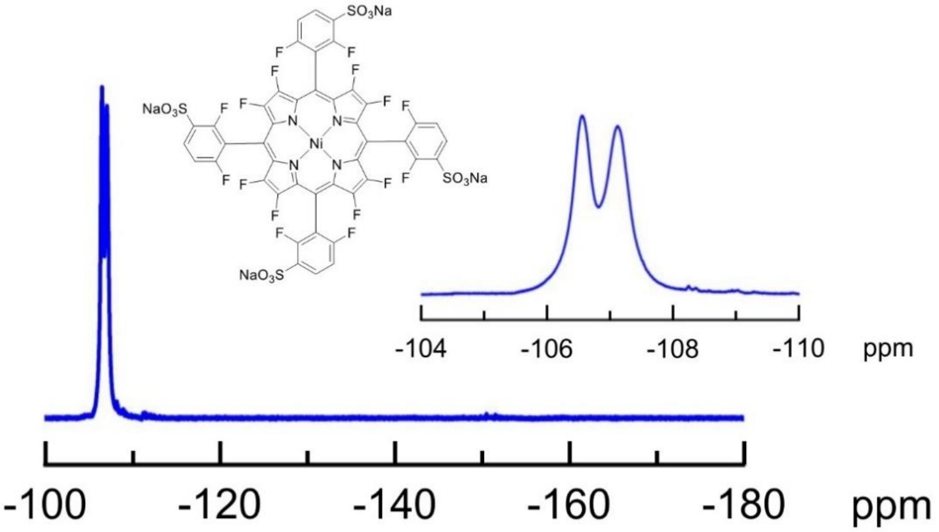

Figure AI.10 *^{19}F NMR of $Na_4[Ni\text{-}F16P]$ in CD_3OD.*

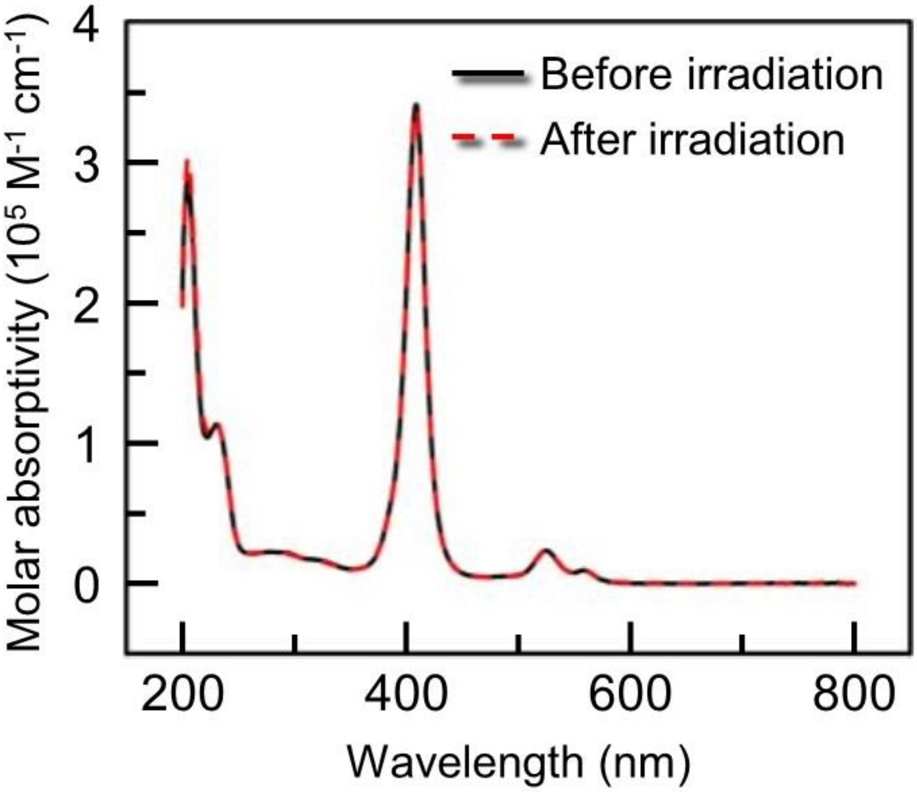

Figure AI.11 *Absorption spectra of [Ni-OMeP]$^{4-}$ before (black solid) and after (red dash) 3 hours irradiation (LED, 450 nm, 15.8 mW) in phosphate buffer (0.1 M, pH 7.0) under air, T = 298 K.*

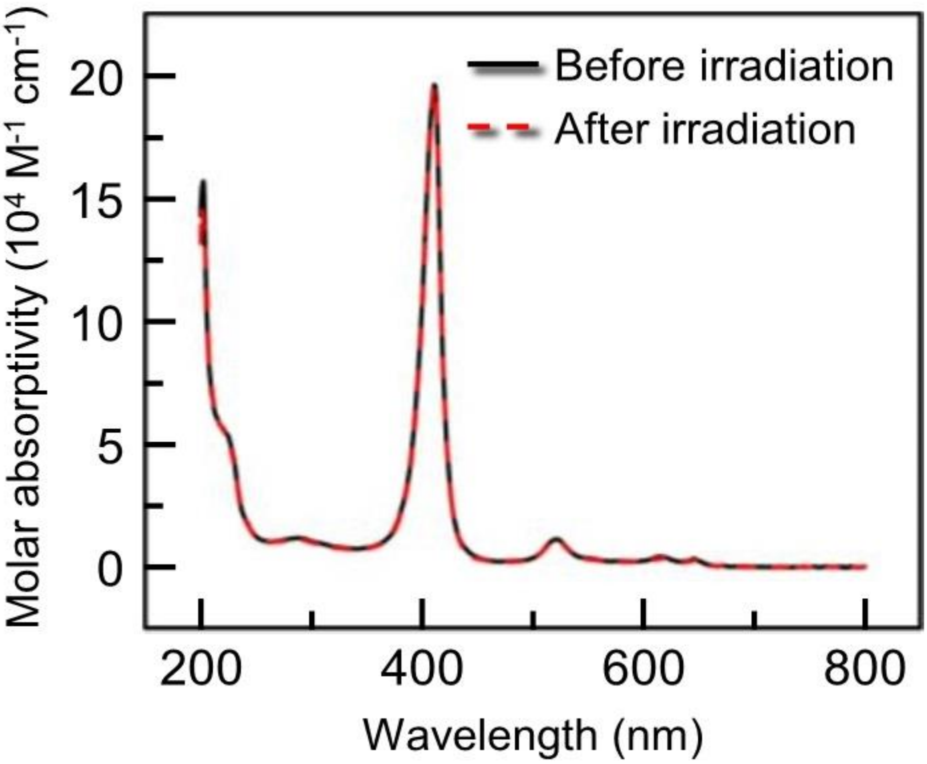

Figure AI.12 *Absorption spectra of [Ni-MeP]$^{4-}$ before (black solid) and after (red dash) 3 hours irradiation (LED, 450 nm, 15.8 mW) in phosphate buffer (0.1 M, pH 7.0) under air, T = 298 K.*

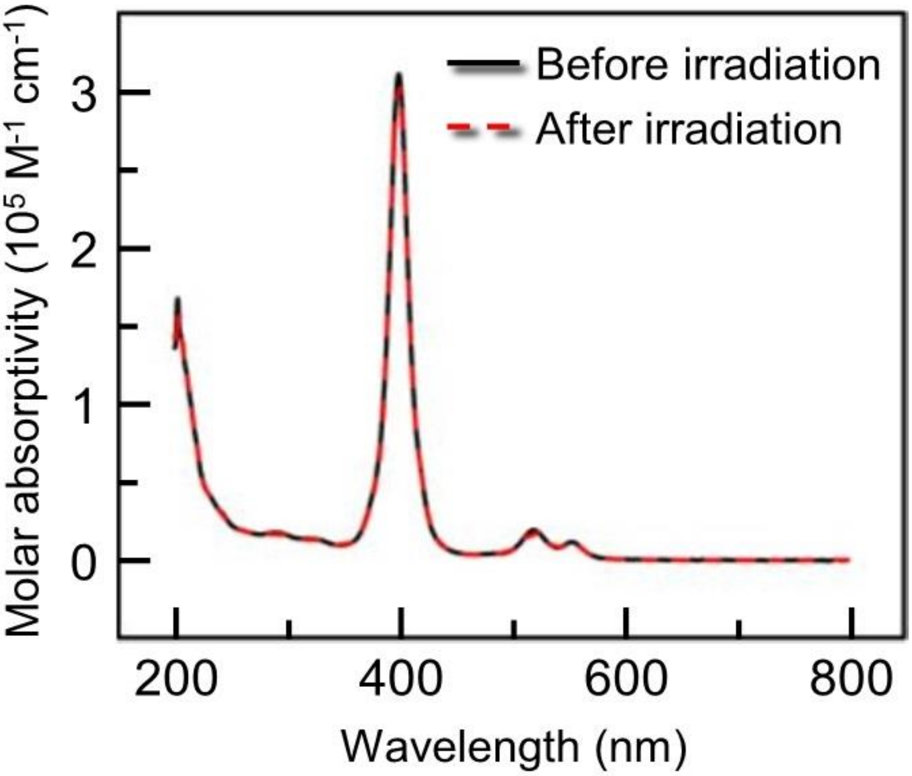

Figure AI.13 *Absorption spectra of [Ni-F8P]$^{4-}$ before (black solid) and after (red dash) 3 hours irradiation (LED, 450 nm, 15.8 mW) in phosphate buffer (0.1 M, pH 7.0) under air, T = 298 K.*

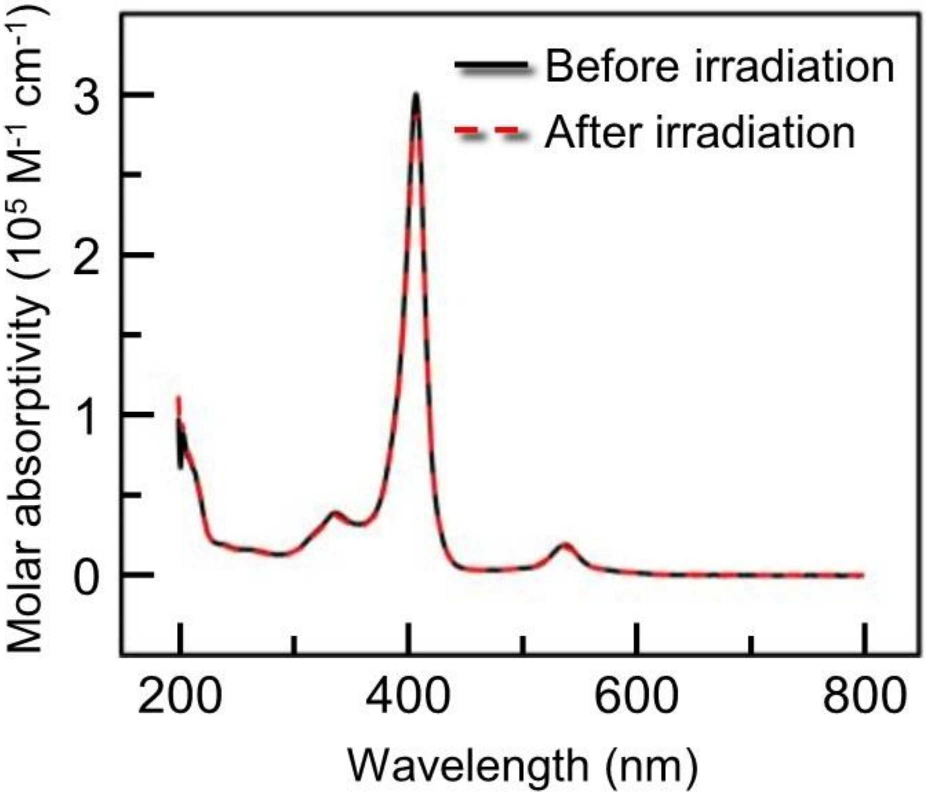

Figure AI.14 *Absorption spectra of [Ni-F16P]$^{4-}$ before (black solid) and after (red dash) 3 hours irradiation (LED, 450 nm, 15.8 mW) in phosphate buffer (0.1 M, pH 7.0) under air, T = 298 K.*

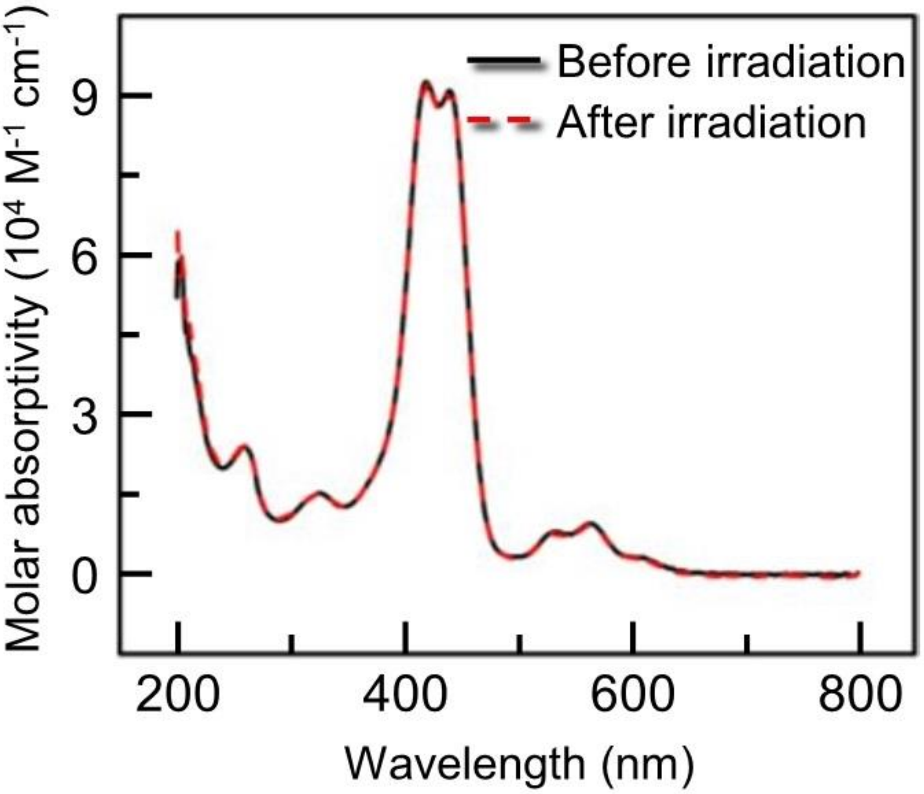

***Figure AI.15** Absorption spectra of [Ni-MPyP]$^{4+}$ before (black solid) and after (red dash) 3 hours irradiation (LED, 450 nm, 15.8 mW) in phosphate buffer (0.1 M, pH 7.0) under air, T = 298 K.*

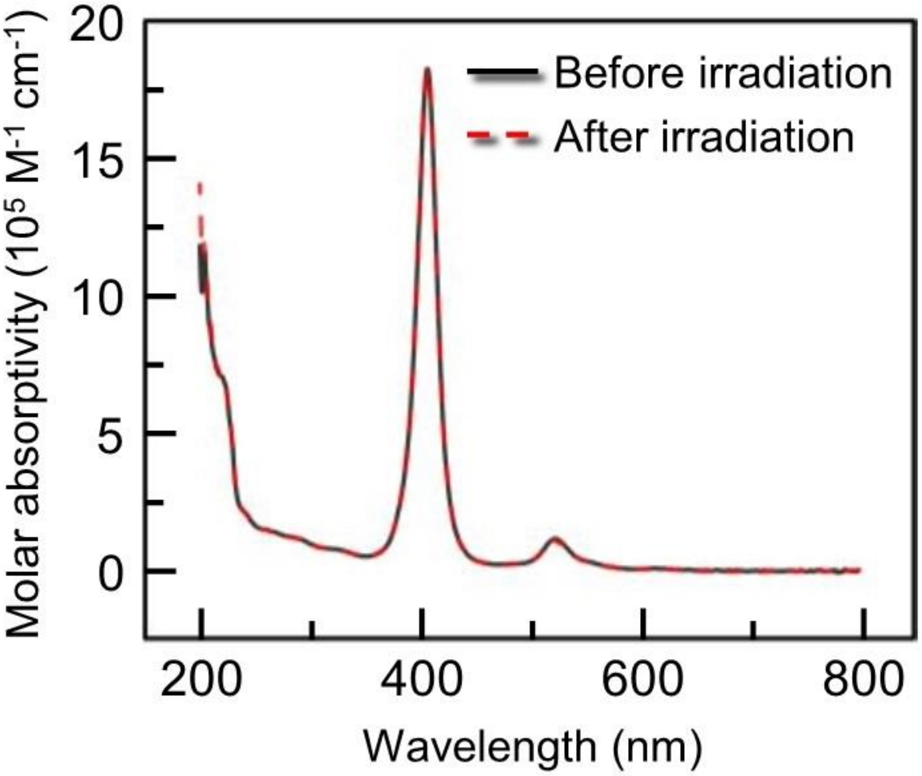

Figure AI.16 *Absorption spectra of [Ni-TMAP]$^{4+}$ before (black solid) and after (red dash) 3 hours irradiation (LED, 450 nm, 15.8 mW) in phosphate buffer (0.1 M, pH 7.0) under air, T = 298 K.*

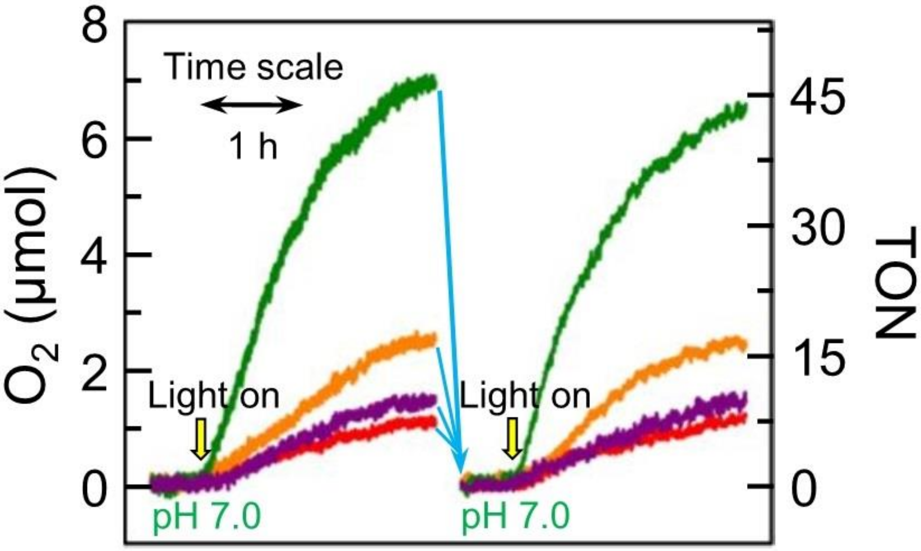

Figure AI.17 *Repetitive photocatalytic water oxidation using a homogeneous mixture containing 0.05 mM [Ni-OMeP]$^{4-}$ (red), [Ni-MeP]$^{4-}$ (orange), [Ni-MPyP]$^{4+}$ (green) or [Ni-TMAP]$^{4+}$ (purple) with 0.67 mM [Ru(bpy)$_3$]Cl$_2$ and 50 mM Na$_2$S$_2$O$_8$ in 0.1 M sodium phosphate* *buffer (initial pH 7.0), using blue light (450 nm, 15.8 mW), T = 298 K. Between the two irradiation experiment, neutralization (cyan arrow) was realized by adding NaOH solid by checking pH, 0.67 mM fresh [Ru(bpy)*$_3$*]Cl*$_2$ *and 50 mM Na*$_2$*S*$_2$*O*$_8$ *as solids were added.*

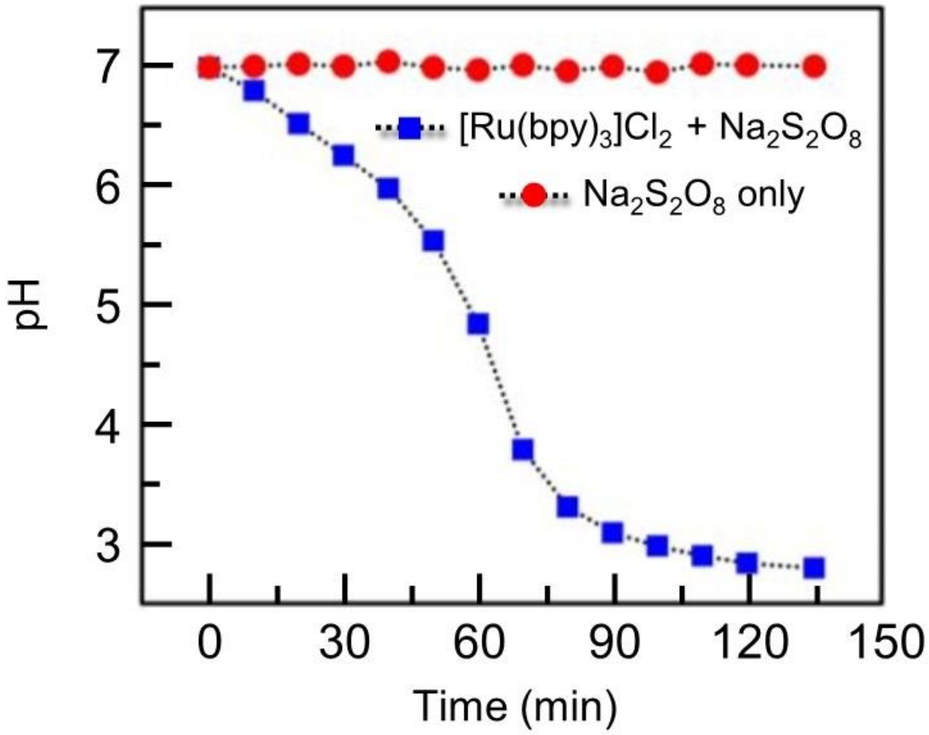

Figure AI.18 *pH change of 0.1 M sodium phosphate buffer (initial pH 7.0) solution containing 50 mM Na*$_2$*S*$_2$*O*$_8$ *(red solid circle) or 0.67 mM [Ru(bpy)*$_3$*]Cl*$_2$ *and 50 mM Na*$_2$*S*$_2$*O*$_8$ *(blue solid square) during blue light (450 nm, 15.8 mW) irradiation, T = 298 K.*

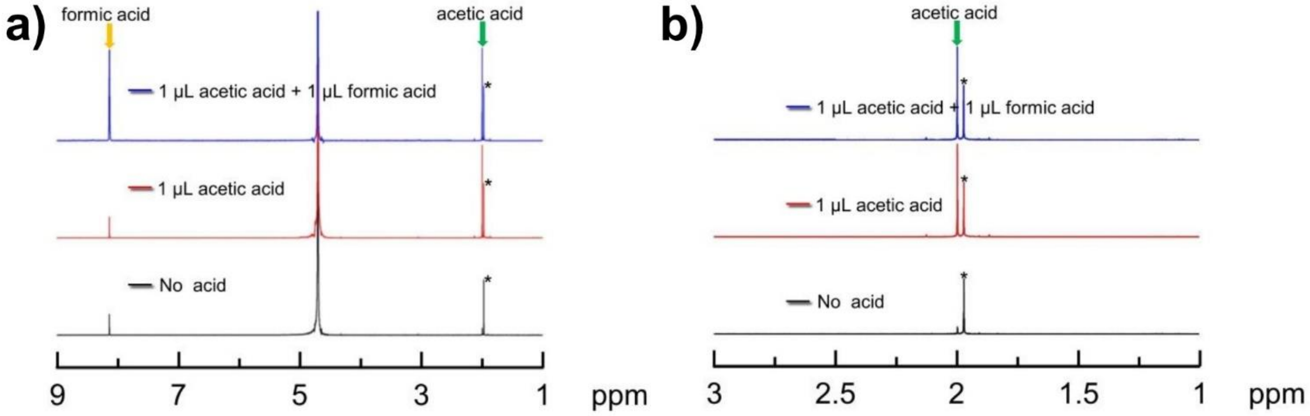

Figure AI.19 *a) ^{1}H NMR of 0.67 mM [Ru(bpy)$_3$]Cl$_2$ and 50 mM Na$_2$S$_2$O$_8$ in D$_2$O after 135 min blue light (450 nm, 15.8 mW) irradiation (black), and adding 1 μL acetic acid (red), 1 μL acetic acid and 1 μL formic acid (blue) into the 0.5 mL D$_2$O solution. b) zoom of spectra shown in a). * represents the 0.5 μL acetonitrile added as internal standard.*

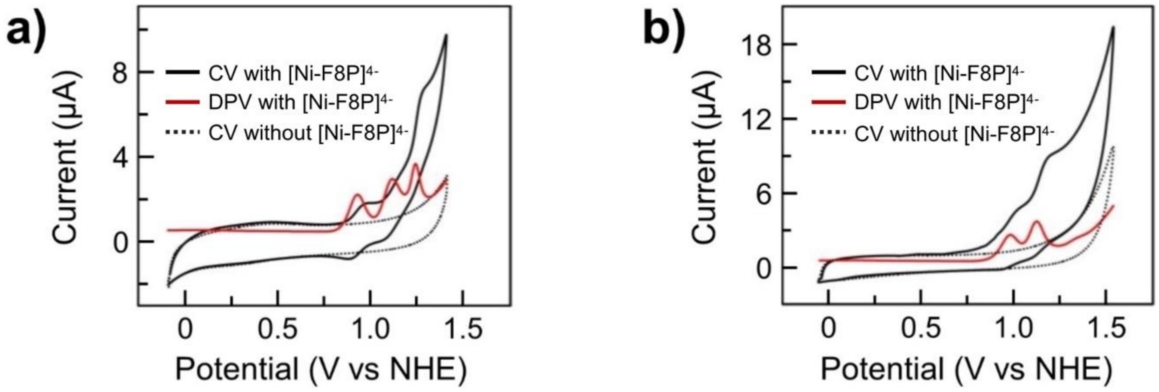

Figure AI.20 *CV and DPV of 0.25 mM [Ni-F8P]$^{4-}$ in 0.1 M a) pH 2.8 and b) pH 7.0 phosphate buffer. Conditions: 0.07 cm^2 working electrode, Pt wire auxiliary electrode, Ag/AgCl reference electrode, 50 mV s^{-1} CV scan rate, T = 298 K. DPV experimental parameters: 0.004 V increase potential, 0.05 V amplitude, 0.05 s pulse width, 0.0167 s sampling width, 0.5 s sample period.*

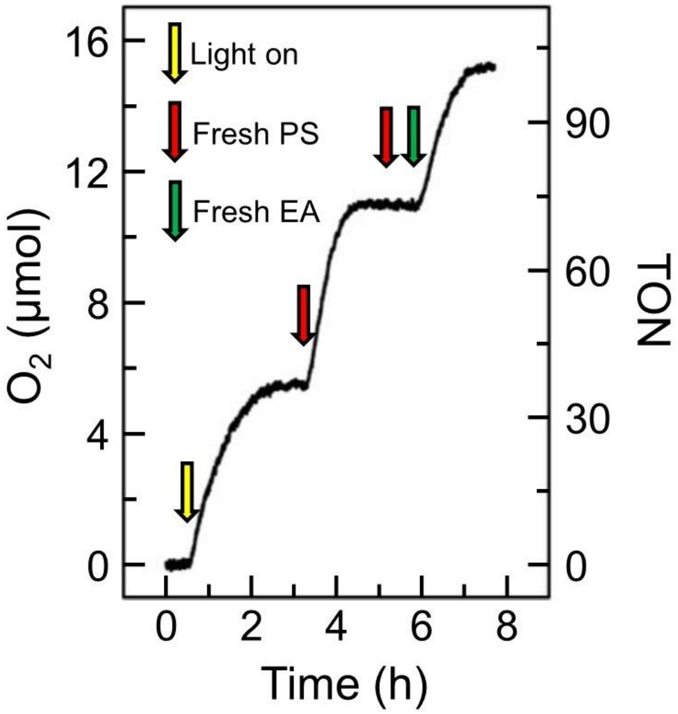

Figure AI.21 *Repetitive photocatalytic water oxidation using a homogeneous mixture containing 0.05 mM [Ni-F8P]$^{4-}$, 0.67 mM [Ru(bpy)$_3$]Cl$_2$ and 50 mM $Na_2S_2O_8$ in 0.1 M sodium phosphate buffer (initial pH 7.0), using LED lamp (450 nm, 15.8 mW), T = 298 K. Fresh 0.67 mM [Ru(bpy)$_3$]Cl$_2$ was added at t = 3.5 h and t = 5.5, another batch of 50 mM $Na_2S_2O_8$ was added at t = 6.0 h.*

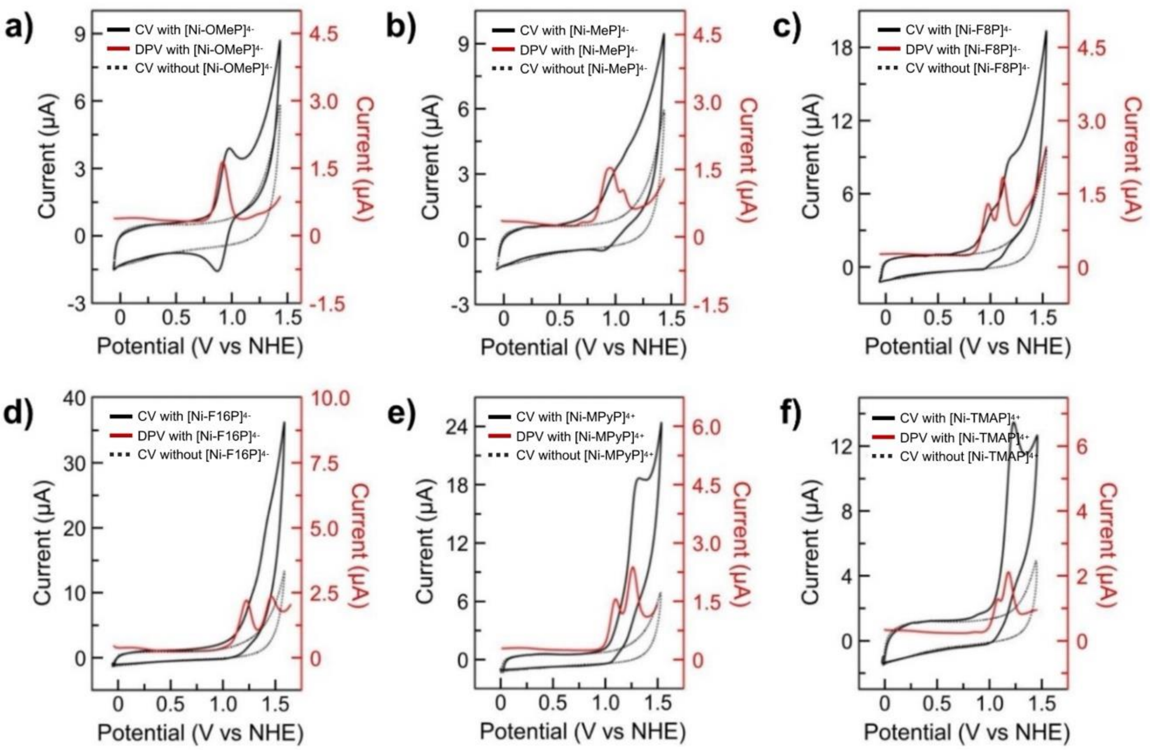

Figure AI.22 *Cyclic voltammetry (CV, black traces) and differential pulse voltammetry (DPV, red traces) of aqueous solutions of a) [Ni-OMeP]$^{4-}$, b) [Ni-MeP]$^{4-}$, c) [Ni-F8P]$^{4-}$, d) [Ni-F16P]$^{4-}$, e) [Ni-MPyP]$^{4+}$, and f) [Ni-TMAP]$^{4+}$ (concentration: 0.25 mM) in 0.1 M phosphate buffer (pH 7.0). Conditions: 0.07 cm^{2} working electrode, Pt wire auxiliary electrode, Ag/AgCl reference electrode, CV scan rate 50 mV s^{-1}, T = 298 K. DPV experimental parameters: 0.004 V increase potential, 0.05 V amplitude, 0.05 s pulse width, 0.0167 s sampling width, 0.5 s sample period.*

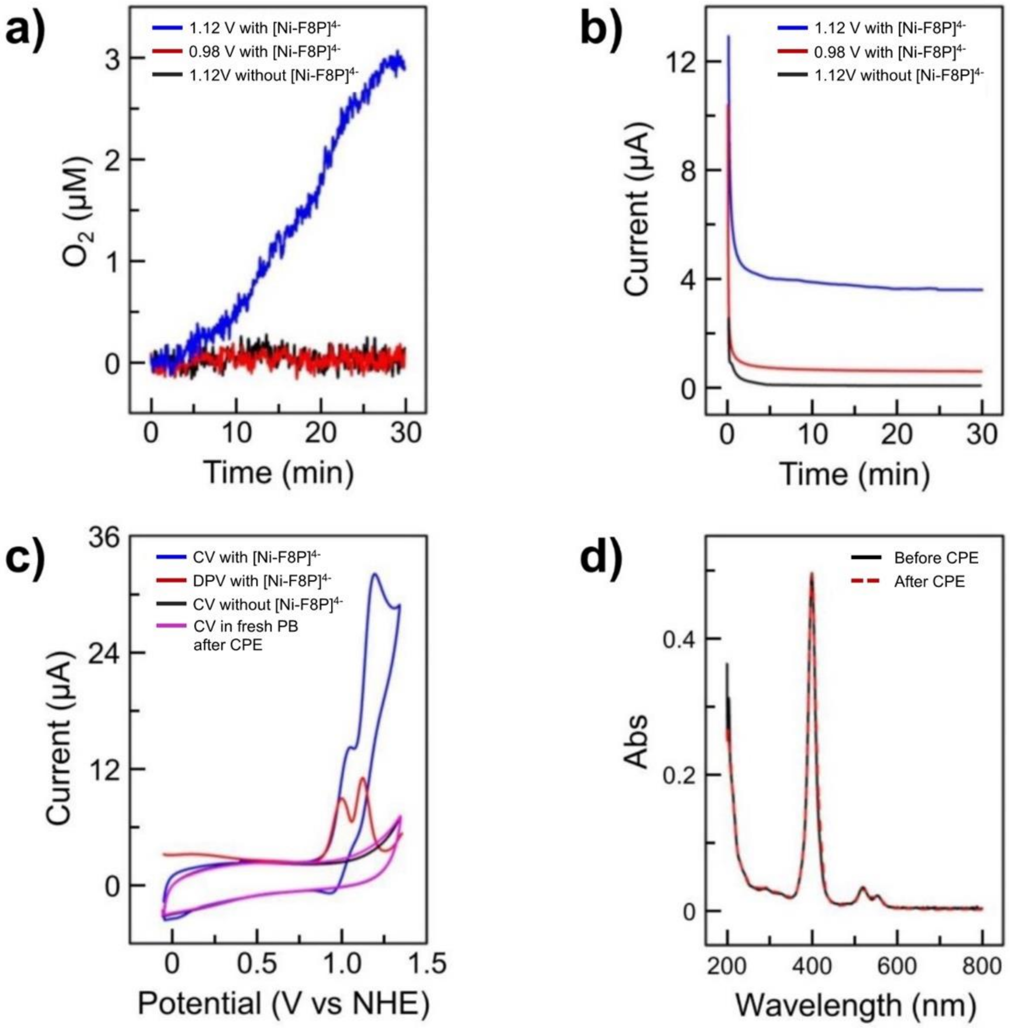

Figure AI.23 *a) The oxygen evolution of the catalytic system comprising [Ni-F8P]$^{4-}$ as determined with CPE. b) Controlled potential electrolysis of a GC electrode with under 0.98 V and 1.12 V (vs NHE) and without 2 mM [Ni-F8P]$^{4-}$ at 1.12 V (vs NHE) in 0.1 M phosphate buffer (pH 7.0). c) CV (blue) and DPV (red) of a freshly cleaned GC electrode with 2 mM [Ni-F8P]$^{4-}$ and CV of a GC electrode without 2 mM [Ni-F8P]$^{4-}$ before (black) and after (magenta) 30 min electrolysis under 1.12 V (vs NHE) with 2 mM [Ni-F8P]$^{4-}$ in 0.1 M phosphate buffer (pH 7.0). d) UV-vis spectra of the solution before and after CPE at 1.12 V (vs NHE), diluted 1000 times by 0.1 M phosphate buffer (pH 7.0). Conditions: 0.07 cm^2 working electrode, Pt wire auxiliary electrode, Ag/AgCl reference electrode, 50 mV s^{-1} CV scan rate, T = 298 K. DPV experimental parameters: 0.004 V increase potential, 0.05 V amplitude, 0.05 s pulse width, 0.0167 s sampling width, 0.5 s sample period. Clark oxygen electrode were set in solution.*

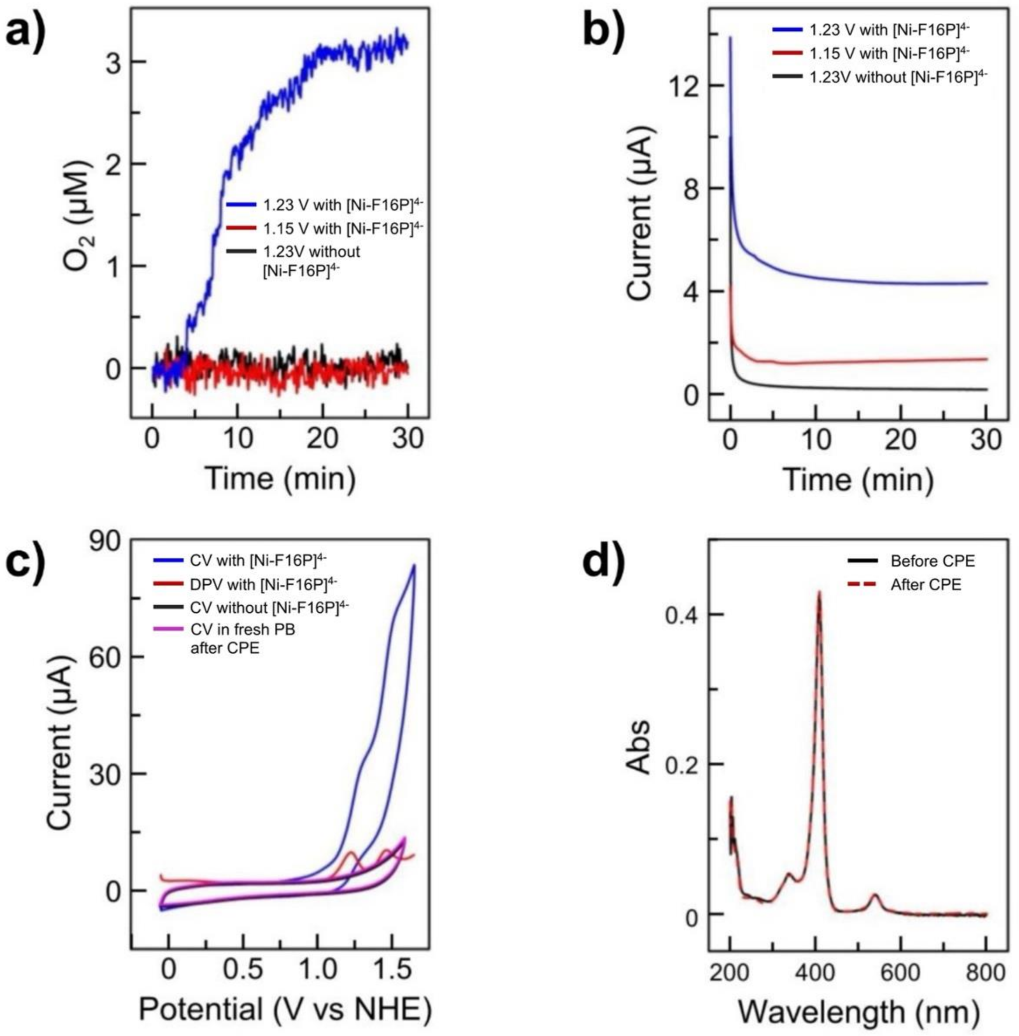

Figure AI.24 *a) The oxygen evolution of the catalytic system comprising [Ni-F16P]*$^{4-}$ *as determined with CPE. b) Controlled potential electrolysis of a GC electrode with under 1.15 V and 1.23 V (vs NHE) and without 2 mM [Ni-F16P]*$^{4-}$ *under 1.23 V (vs NHE) in 0.1 M phosphate buffer (pH 7.0). c) CV (blue) and DPV (red) of a freshly cleaned GC electrode with 2 mM [Ni-F16P]*$^{4-}$ *and CV of a GC electrode without 2 mM [Ni-F16P]*$^{4-}$ *before (black) and after (magenta) 30 min electrolysis under 1.23 V (vs NHE) with 2 mM [Ni-F16P]*$^{4-}$ *in 0.1 M phosphate buffer (pH 7.0). d) UV-vis spectra of the solution before and after CPE at 1.12 V (vs NHE), diluted 1000 times by 0.1 M phosphate buffer (pH 7.0). Conditions: 0.07 cm*^{2} *working electrode, Pt wire auxiliary electrode, Ag/AgCl reference electrode, 50 mV s*$^{-1}$ *CV scan rate, T = 298 K. DPV experimental parameters: 0.004 V increase potential, 0.05 V amplitude, 0.05 s pulse width, 0.0167 s sampling width, 0.5 s sample period. Clark oxygen electrode were set in solution.*

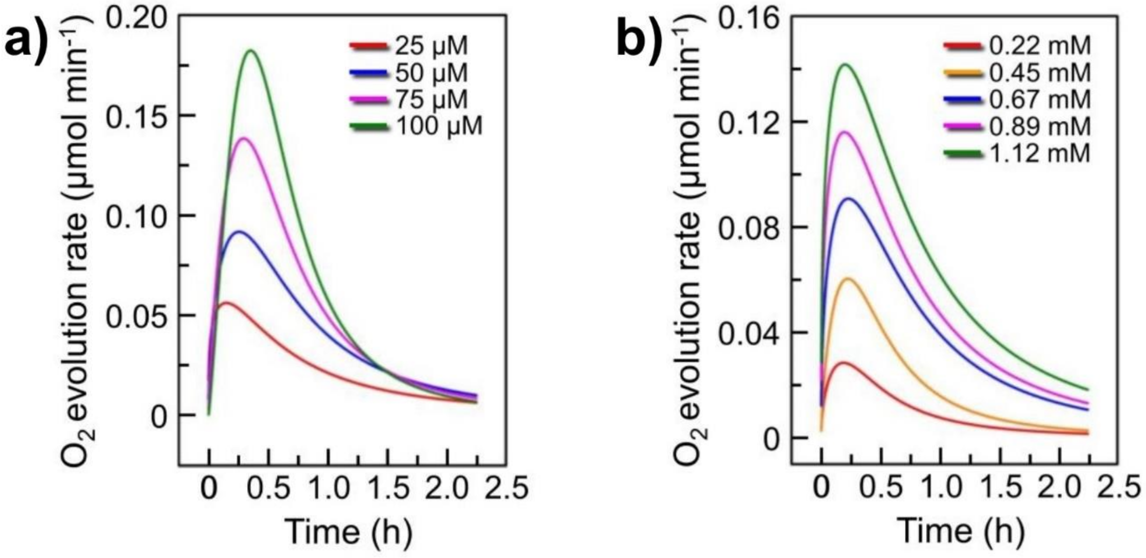

Figure AI.25 *The calculated O_2 evolution rate vs. time during photocatalytic water oxidation in presence of a) different concentrations of $[Ni\text{-}F8P]^{4-}$ with 0.67 mM $[Ru(bpy)_3]Cl_2$ and 50 mM $Na_2S_2O_8$ and b) 0.05 mM $[Ni\text{-}F8P]^{4-}$ with different concentrations of $[Ru(bpy)_3]Cl_2$ and 50 mM $Na_2S_2O_8$ in 0.1 M sodium phosphate buffer (initial pH 7.0), using LED lamp (450 nm, 15,8 mW), T = 298 K.*

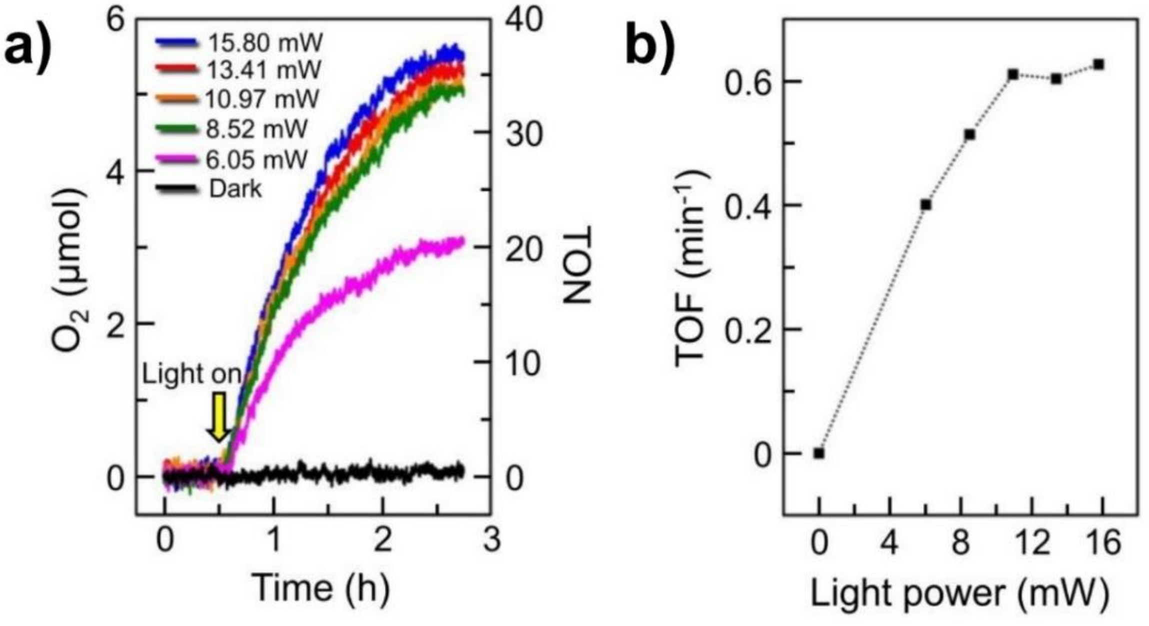

Figure AI.26 *a) Dioxygen evolution during photocatalytic water oxidation in presence of 0.05 mM $[Ni\text{-}F8P]^{4-}$ with 0.67 mM $[Ru(bpy)_3]Cl_2$ and 50 mM $Na_2S_2O_8$ in 0.1 M sodium phosphate buffer (initial pH 7.0), using LED lamp (450 nm) with different optical power, T = 298 K. b) The maximun TOF of the O_2 evolution plotted as a function of the light power.*

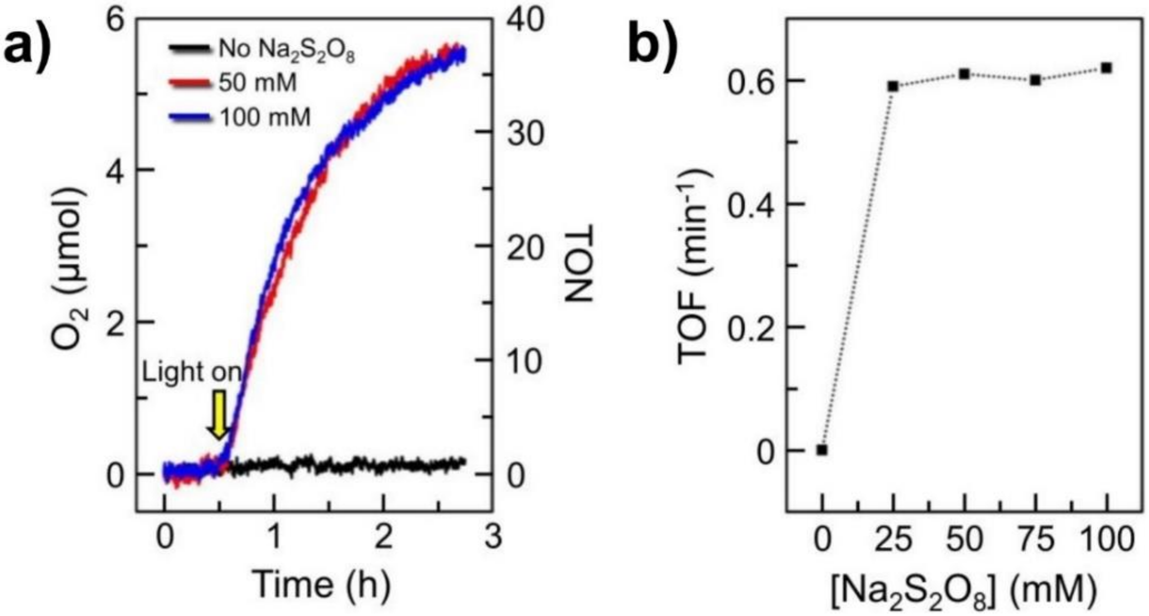

Figure AI.27 *a) Dioxygen evolution during photocatalytic water oxidation in presence of 0.05 mM [Ni-F8P]$^{4-}$ with 0.67 mM [Ru(bpy)$_3$]Cl$_2$ and 0, 50 mM and 100 mM $Na_2S_2O_8$ in 0.1 M sodium phosphate buffer (initial pH 7.0), using LED lamp (450 nm, 15.8 mW), T = 298 K. b) The maximum TOF of the O_2 evolution plotted as a function of the concentration of $Na_2S_2O_8$.*

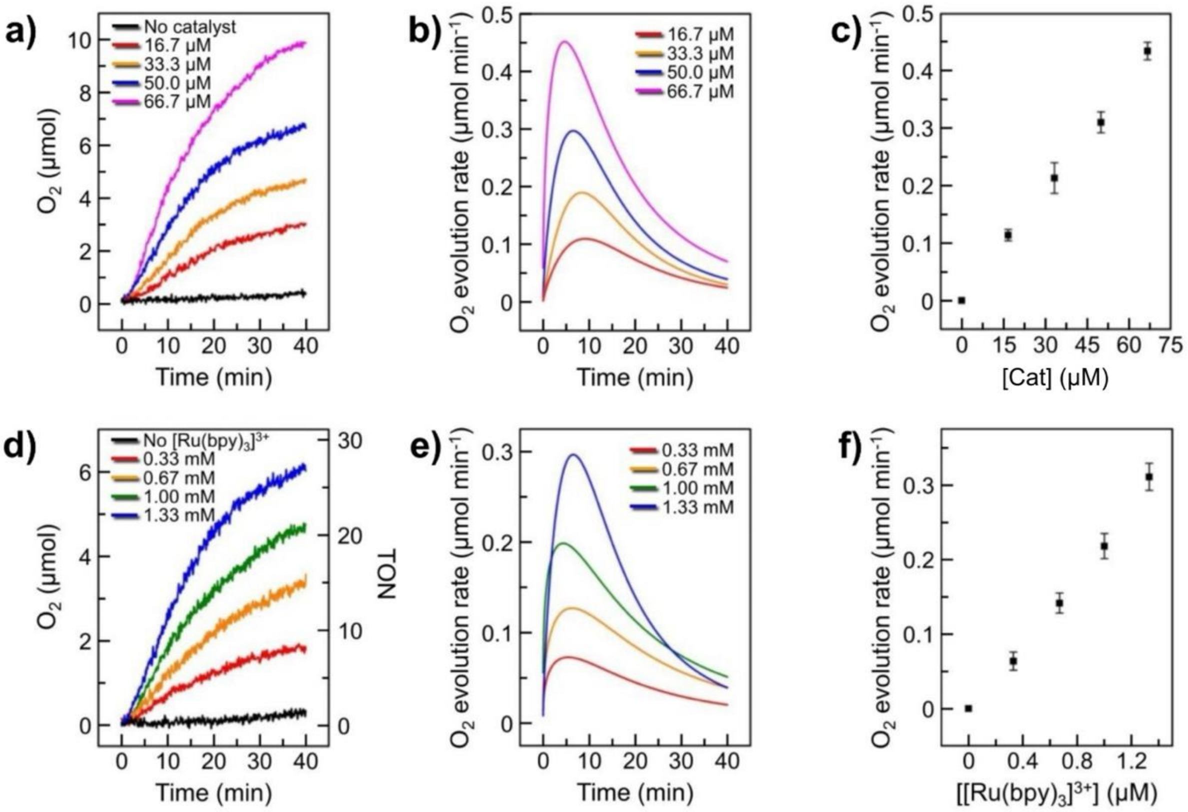

Figure AI.28 *Catalytic oxygen evolution vs. time driven by chemically prepared $[Ru(bpy)_3](ClO_4)_3$. a) different concentrations of $[Ni\text{-}F8P]^{4-}$ with 1.33 mM $[Ru(bpy)_3](ClO_4)_3$ as chemical oxidant, and d) different concentrations of $[Ru(bpy)_3](ClO_4)_3$ with 0.05 mM $[Ni\text{-}F8P]^{4-}$ as WOC in 0.1 M sodium phosphate buffer (initial pH 7.0), T = 298 K. b) and e) the calculated O_2 evolution rate vs. time of a) and d). c) and f) the maximum O_2 evolution rate during catalytic O_2 evolution plotted as a function of c) the concentration of $[Ni\text{-}F8P]^{4-}$ and f) the concentration of $[Ru(bpy)_3](ClO_4)_3$.*

Figure AI.29 *The photocatalytic set-up.*

Table AI.1 *DPV oxidation wave potentials of Ni-porphyrin complexes and $[Ru(bpy)_3]Cl_2$*

	$[Ni\text{-}OMeP]^{4-}$	**$[Ni\text{-}MeP]^{4-}$**	**$[Ni\text{-}F8P]^{4-}$**	**$[Ni\text{-}F16P]^{4-}$**	**$[Ni\text{-}MPyP]^{4+}$**	**$[Ni\text{-}TMAP]^{4+}$**	**$[Ru(bpy)_3]^{2+}$**
First oxidation	0.92 V	0.96 V	0.98 V	1.23 V	1.10 V	0.91 V	1.26 V
Second oxidation		1.07 V	1.12 V	1.46 V	1.25 V	1.01 V	

Potentials versus NHE, DPV measurements were measured in pH 7.0 sodium phosphate buffer, 298

APPENDIX II: SUPPORTING INFORMATION FOR CHAPTER 3

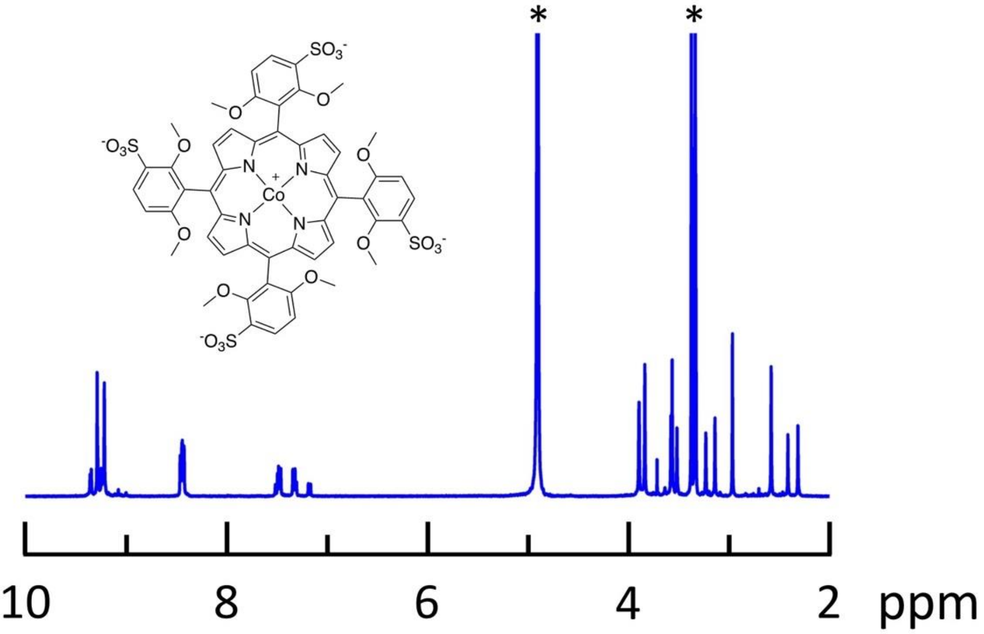

Figure AII.1 *^{1}H NMR of [Co-OMeP]$^{3-}$ in MeOD. * Methanol and water.*

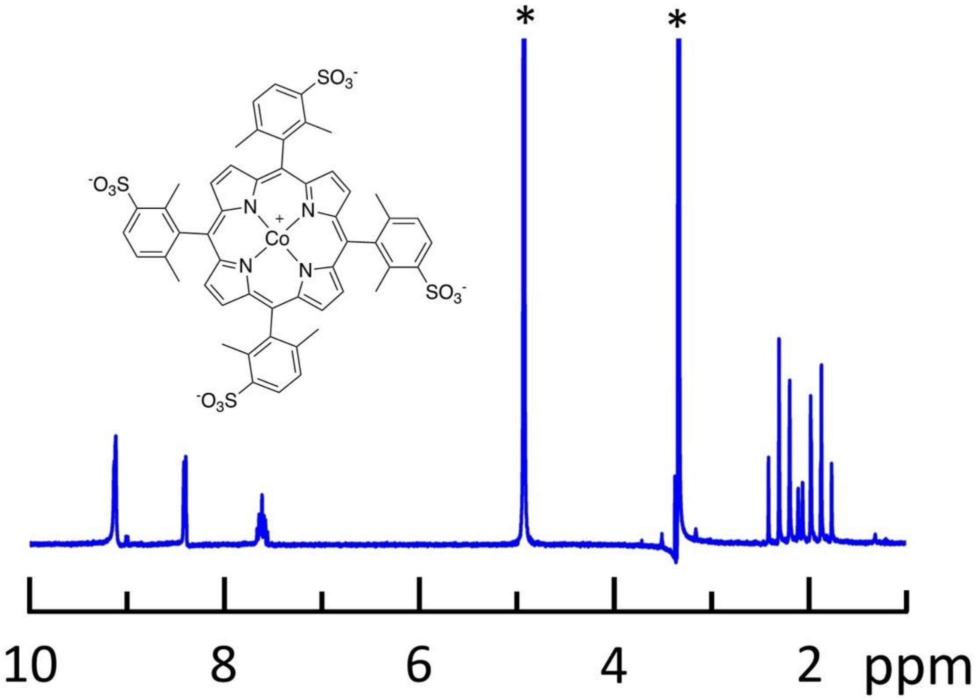

Figure AII.2 *^{1}H NMR of [Co-MeP]$^{3-}$ in MeOD. * Methanol and water.*

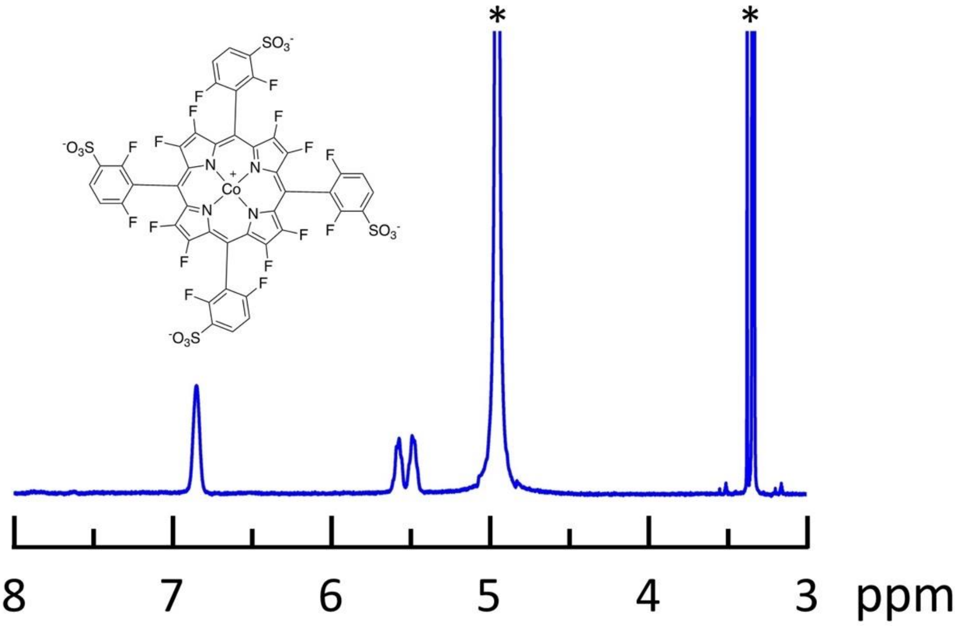

Figure AII.3 *^{1}H NMR of [Co-F16P]$^{3-}$ in MeOD. * Methanol and water.*

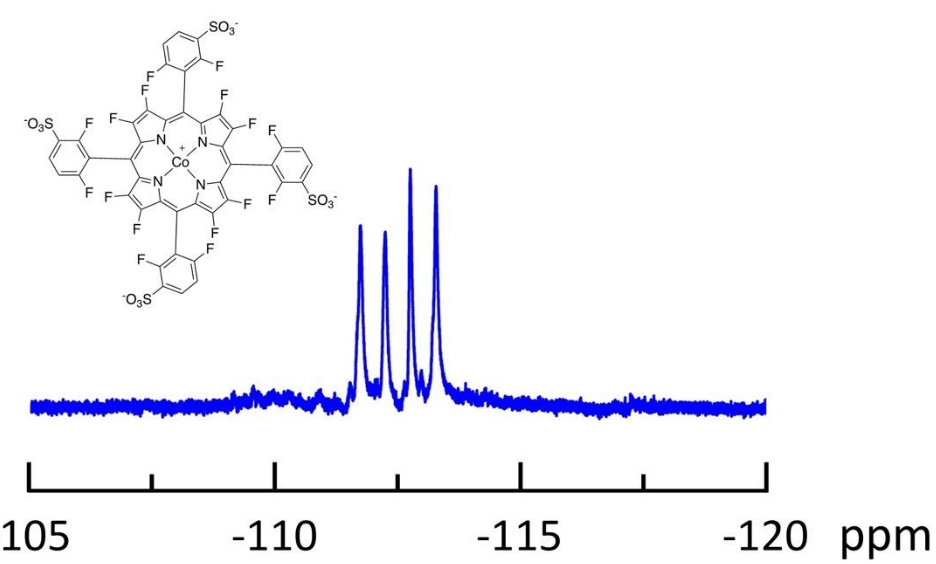

Figure AII.4 *^{19}F NMR of [Co-F16P]$^{3-}$ in MeOD.*

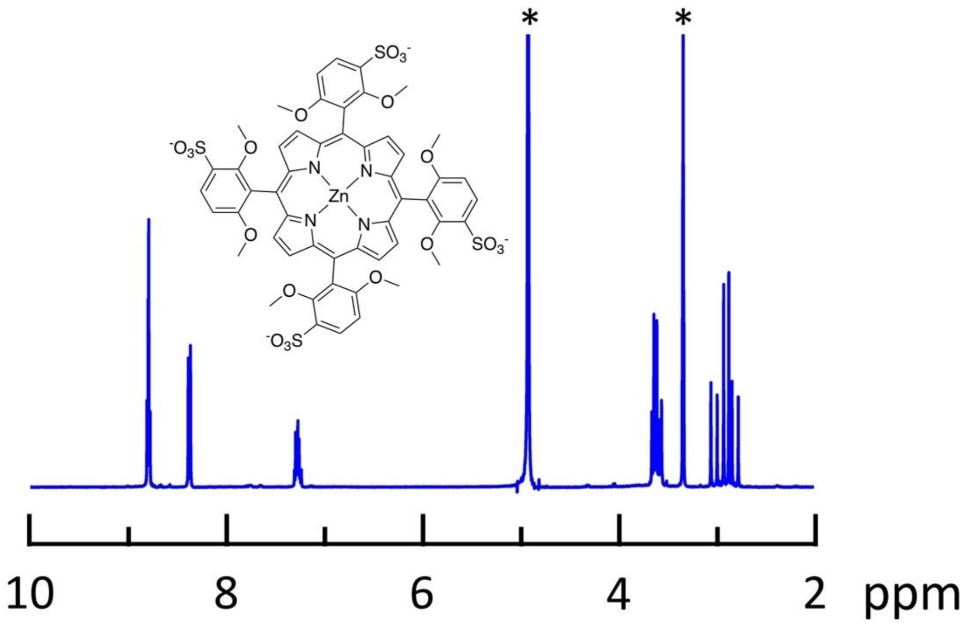

Figure AII.5 *^{1}H NMR of [Zn-OMeP]$^{4-}$ in MeOD. * Methanol and water.*

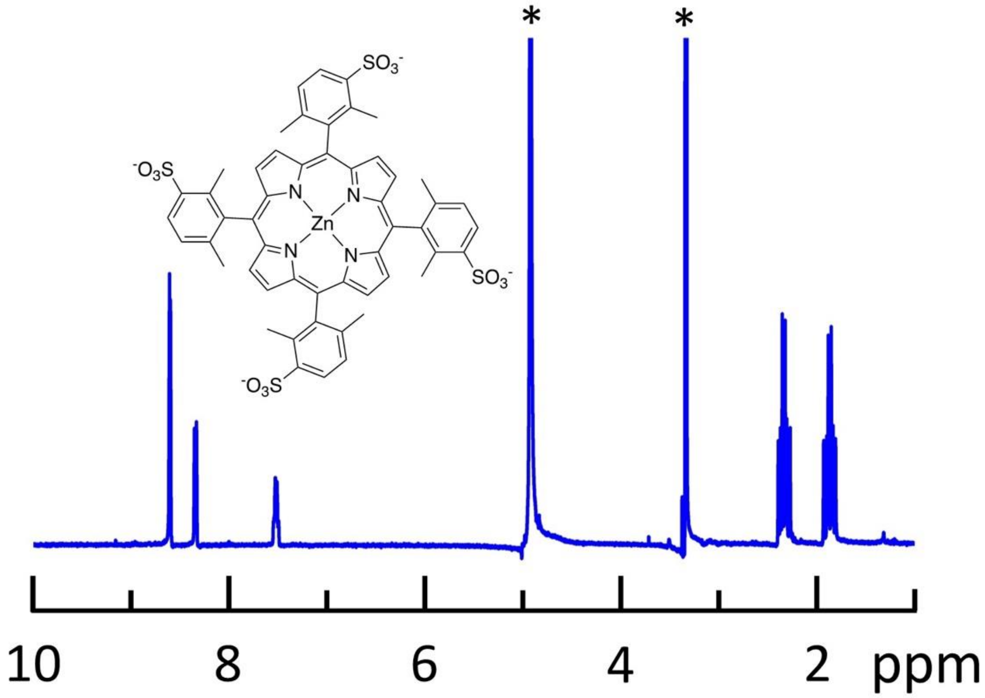

Figure AII.6 *^{1}H NMR of [Zn-MeP]$^{4-}$ in MeOD. * Methanol and water.*

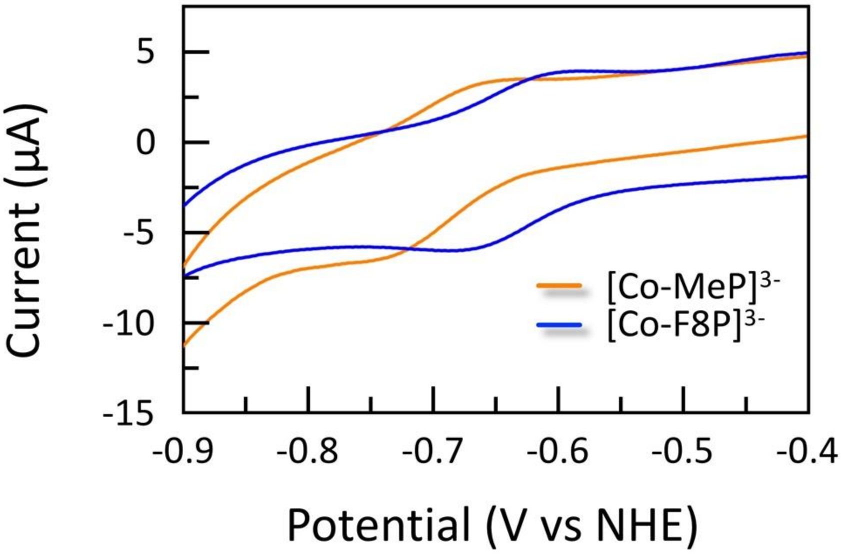

Figure AII.7 *Cyclic voltammetry from –0.9 to –0.4 V vs. NHE of the [Co-MeP]$^{3-}$ and [Co-MeP]$^{3-}$ in Figure 3.3b.*

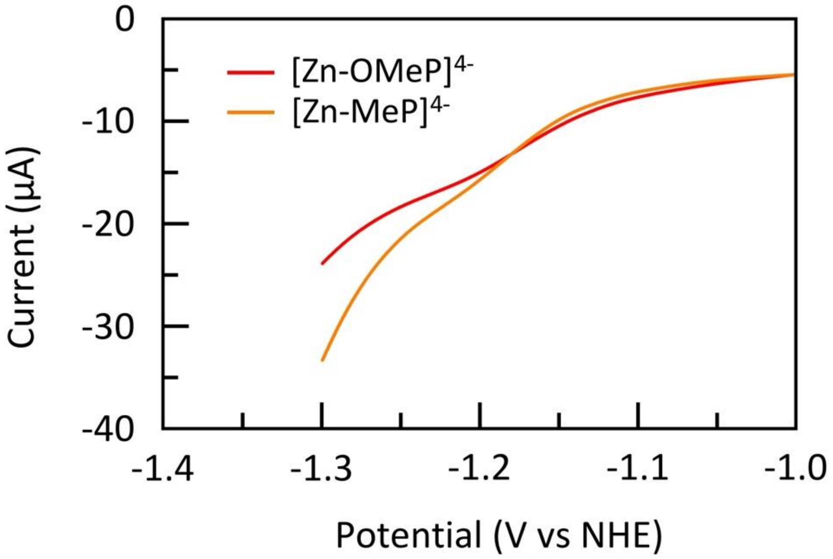

Figure AII.8 *Linear sweep voltammetry from –1.3 to –1.0 V vs. NHE of the [Zn-OMeP]$^{4-}$ and [Zn-MeP]$^{4-}$ in Figure 3.3c.*

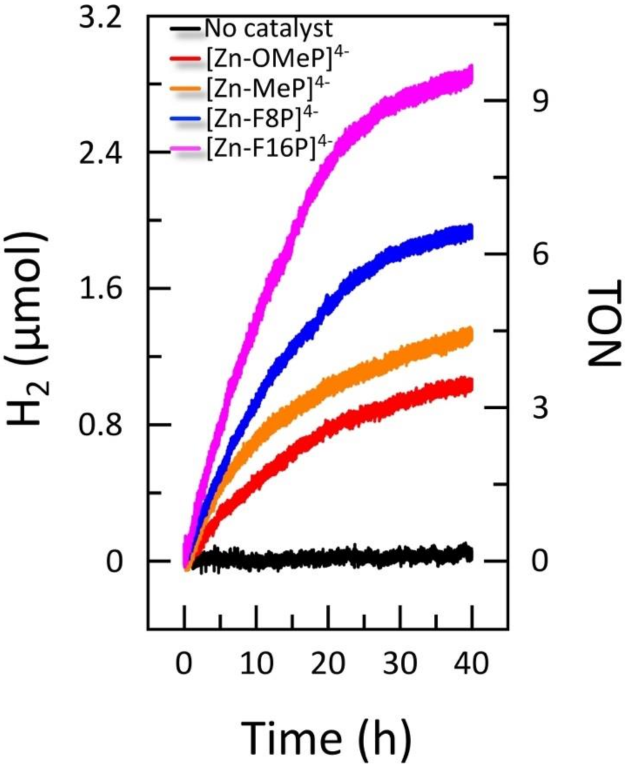

Figure AII.9 *Hydrogen evolution during photocatalytic water reduction in presence of 0.1 mM catalyst [Zn-OMeP]$^{4-}$, [Zn-MeP]$^{4-}$, [Zn-F8P]$^{4-}$ and [Zn-F16P]$^{4-}$, using 0.5 mM [Ru(bpy)$_3$]Cl$_2$ as photosensitizer, 0.1 M ascorbate and TCEP, in pH 7.0 aqueous solution, and LED lamp (450 nm, 16 mW) for irradiation, T = 298 K.*

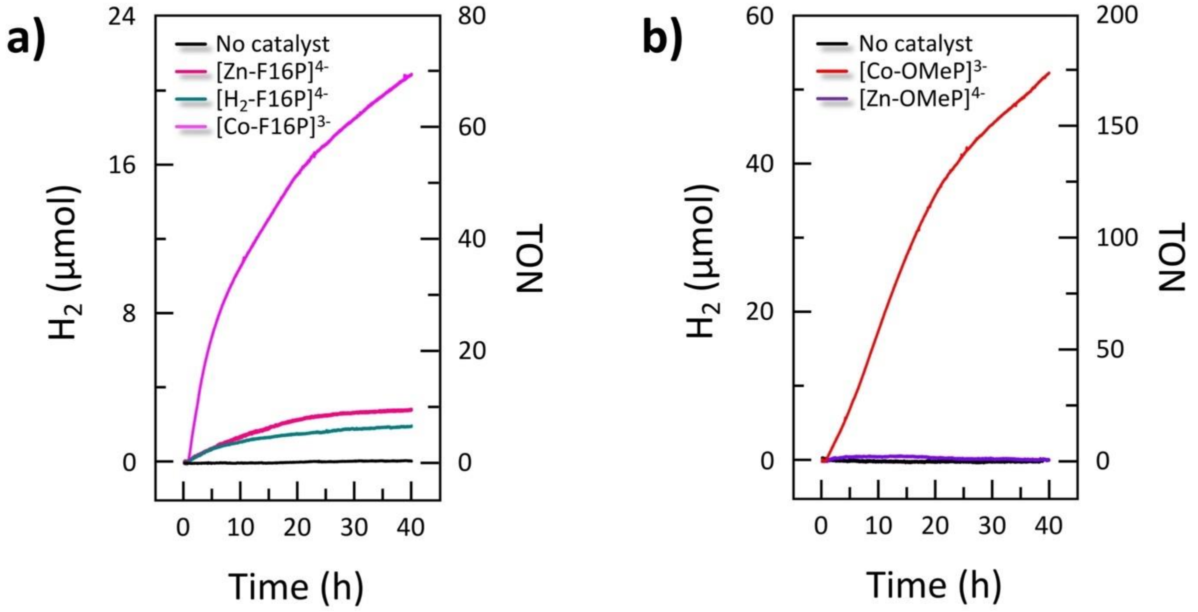

Figure AII.10 *Hydrogen evolution during photocatalytic water reduction in presence of a) 0.1 mM catalyst [Co-F16P]$^{3-}$, [H$_2$-F16P]$^{4-}$ and [Zn-F16P]$^{4-}$ in pH 7.0 aqueous solution, and b)*

0.1 mM catalyst [Co-OMeP]$^{3-}$ and [Zn-OMeP]$^{4-}$ in pH 4.1 aqueous solution using 0.5 mM [Ru(bpy)$_3$]Cl$_2$ as photosensitizer, 0.1 M ascorbate and TCEP, and LED lamp (450 nm, 16 mW) for irradiation, T = 298 K.

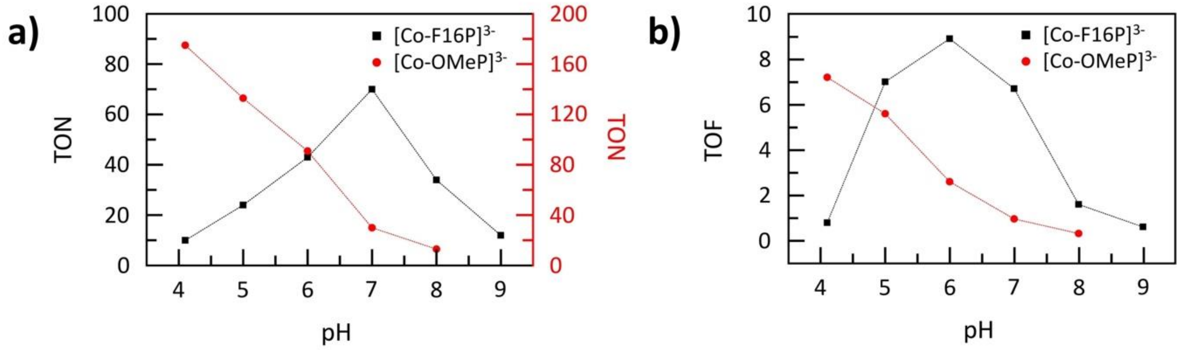

Figure AII.11 a) *Turnover numbers and b) turnover frequencies of photocatalytic H_2 evolution systems in Figure 3.5 plotted as a function of the pH.*

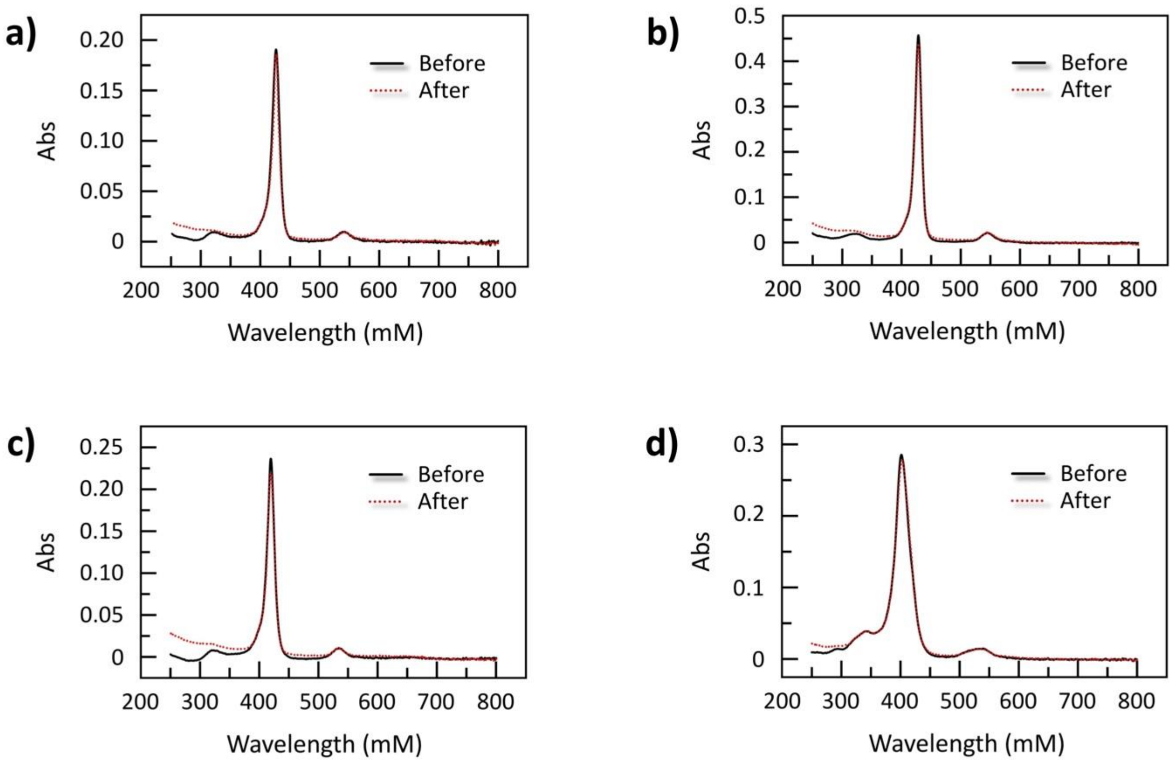

Figure AII.12 *Absorption spectra of 2 μM a) [Co-OMeP]$^{3-}$, b) [Co-MeP]$^{3-}$, 3) [Co-F8P]$^{3-}$, and 4) [Co-F16P]$^{3-}$ before (black solid) and after (red short dot) 48 hours irradiation (LED lamp, 450 nm, 16 mW) in 0.1 M sodium phosphate buffer (pH 7.0) under air, T = 298 K.*

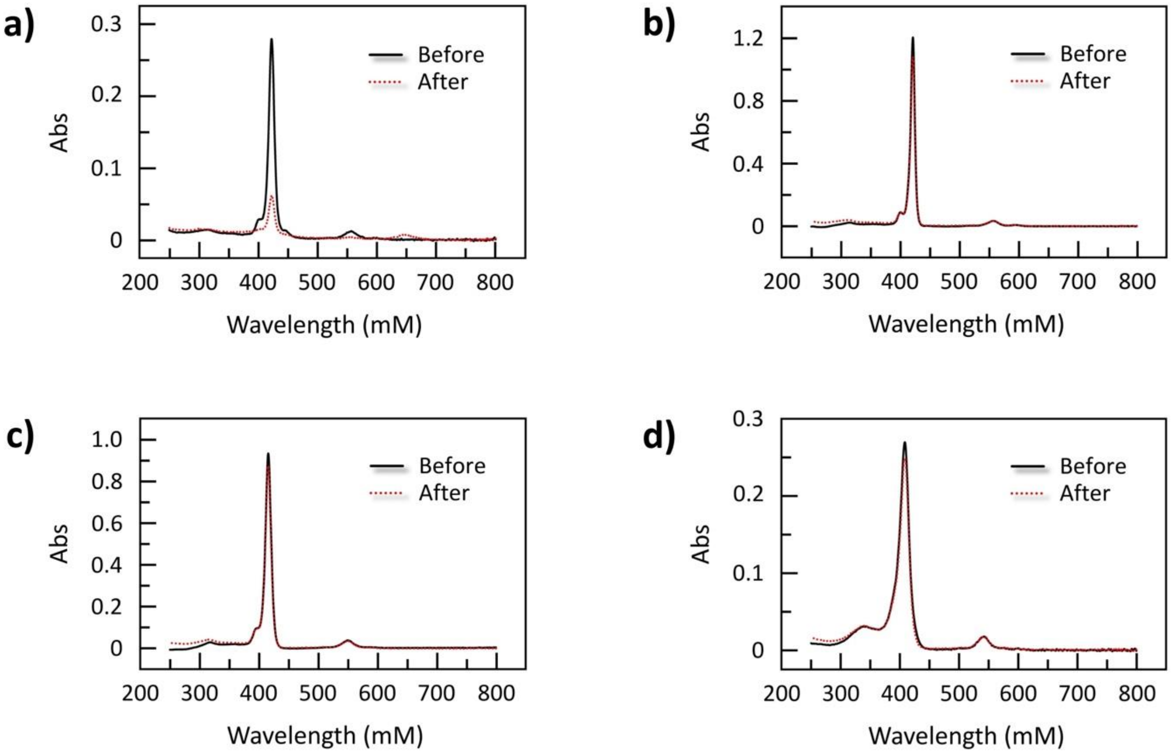

Figure AII.13 Absorption spectra of 2 μM a) $[Zn\text{-}OMeP]^{4-}$, b) $[Zn\text{-}MeP]^{4-}$, 3) $[Zn\text{-}F8P]^{4-}$, and 4) $[Zn\text{-}F16P]^{4-}$ before (black solid) and after (red short dot) 48 hours irradiation (LED lamp, 450 nm, 16 mW) in 0.1 M sodium phosphate buffer (pH 7.0) under air, T = 298 K.

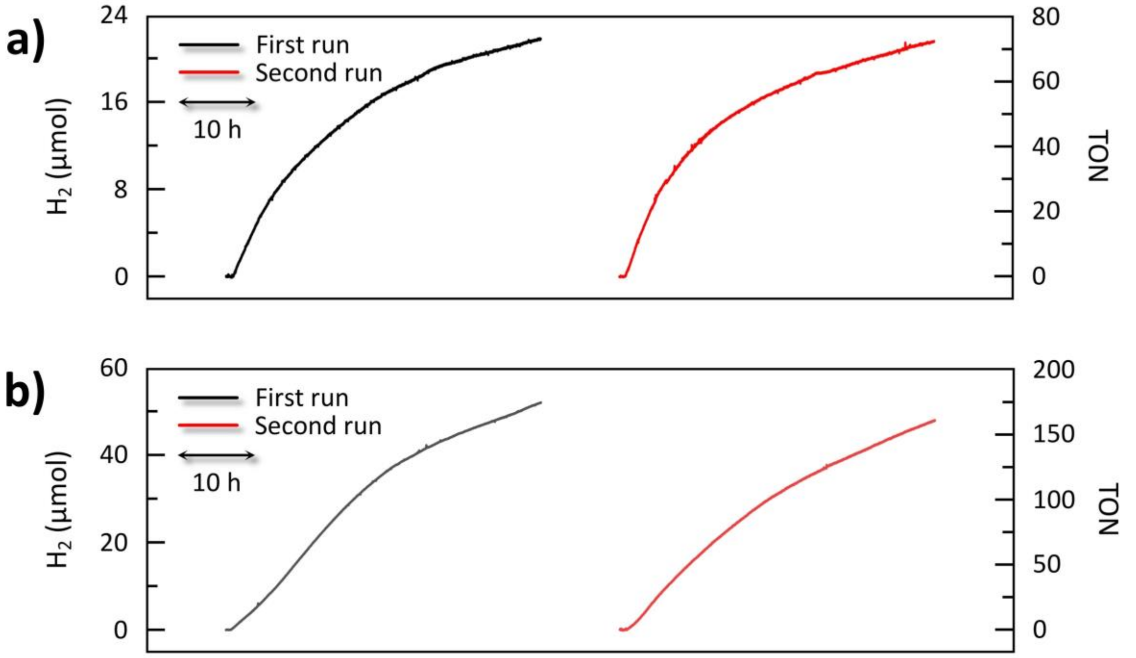

Figure AII.14 *Repetitive photocatalytic hydrogen evolution in presence of a) 0.1 mM [Co-F16P]$^{3-}$ in pH 7.0 and b) [Co-OMeP]$^{3-}$ in different pH 4.1 aqueous solution using 0.5 mM [Ru(bpy)$_3$]Cl$_2$ as photosensitizer, 0.1 M ascorbate and TCEP, and LED lamp (450 nm, 16 mW) for irradiation, T = 298 K. Between the two irradiation experiments, 1.5 μmol fresh [Ru(bpy)$_3$]Cl$_2$ was added as solids.*

APPENDIX III: SUPPORTING INFORMATION FOR CHAPTER 4

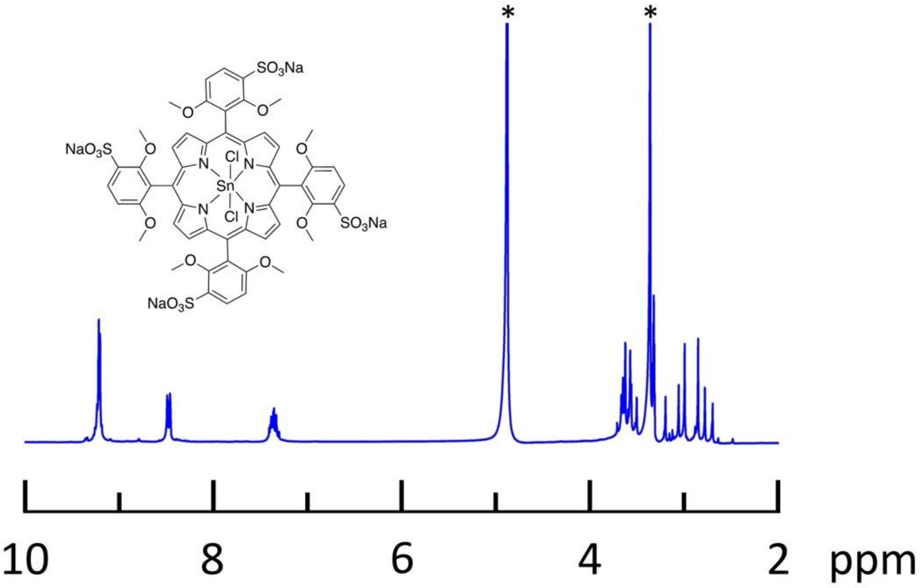

Figure AIII.1 *^{1}H NMR of [Sn-OMeP]$^{4-}$ in MeOD. * Methanol and water.*

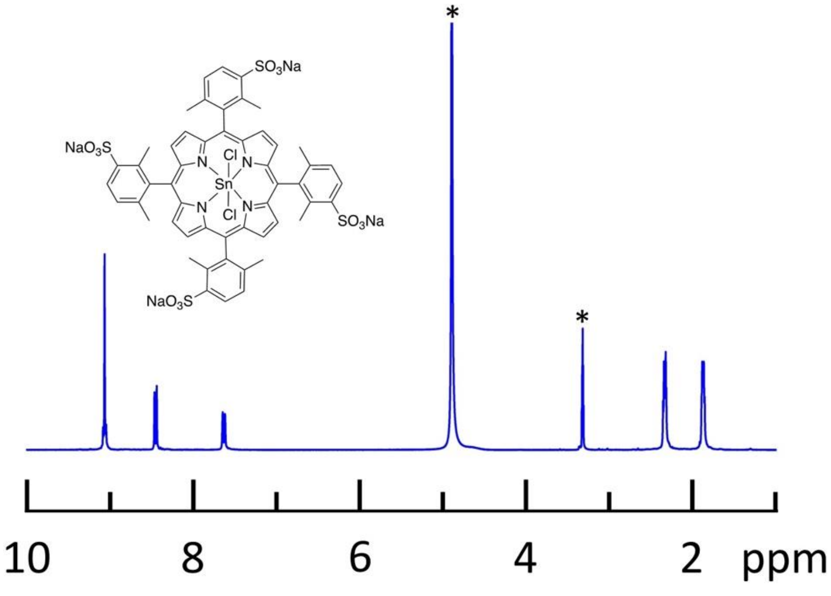

Figure AIII.2 *^{1}H NMR of [Sn-MeP]$^{4-}$ in MeOD. * Methanol and water.*

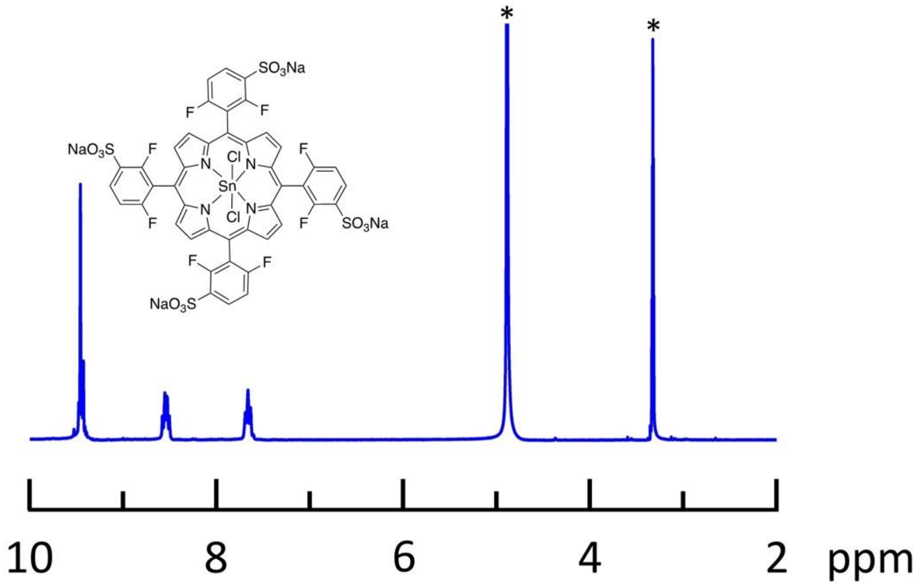

Figure AIII.3 *^{1}H NMR of [Sn-F8P]$^{4-}$ in MeOD. * Methanol and water.*

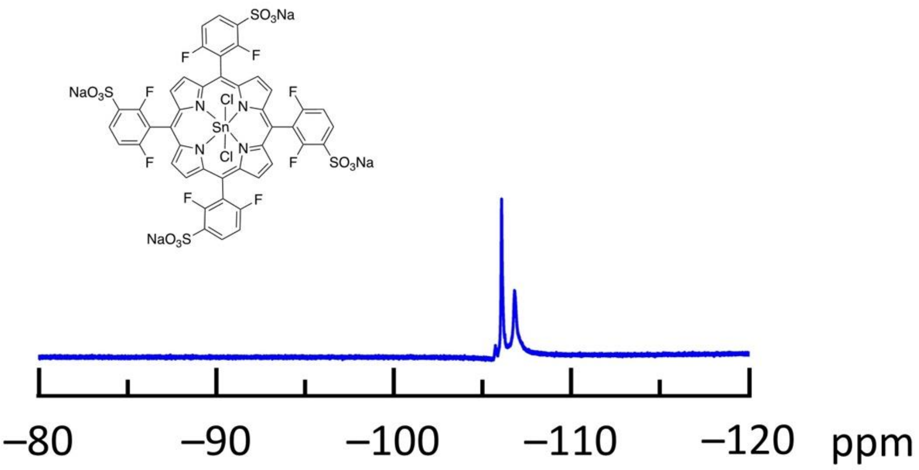

Figure AIII.4 *^{19}F NMR of [Sn-F8P]$^{4-}$ in MeOD.*

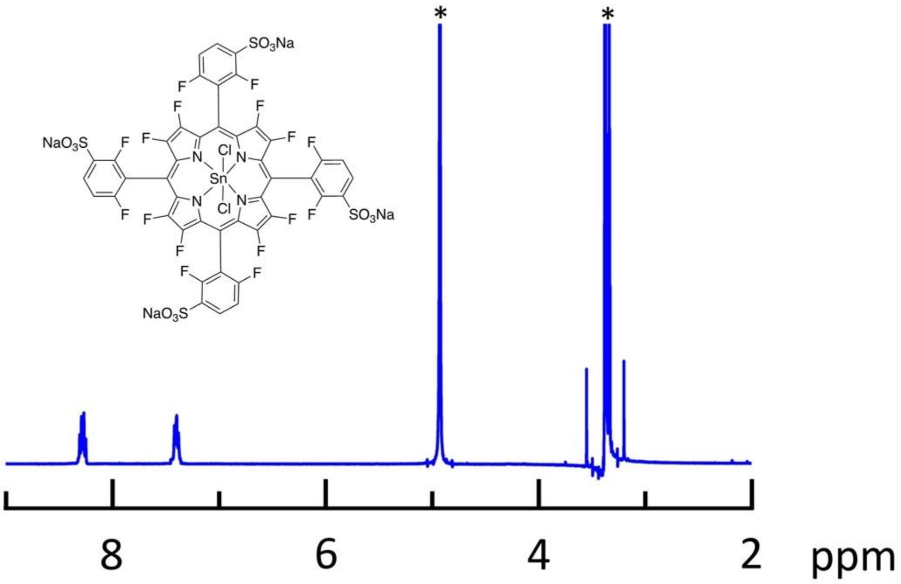

Figure AIII.5 *^{1}H NMR of $[Sn\text{-}F16P]^{4-}$ in MeOD. * Methanol and water.*

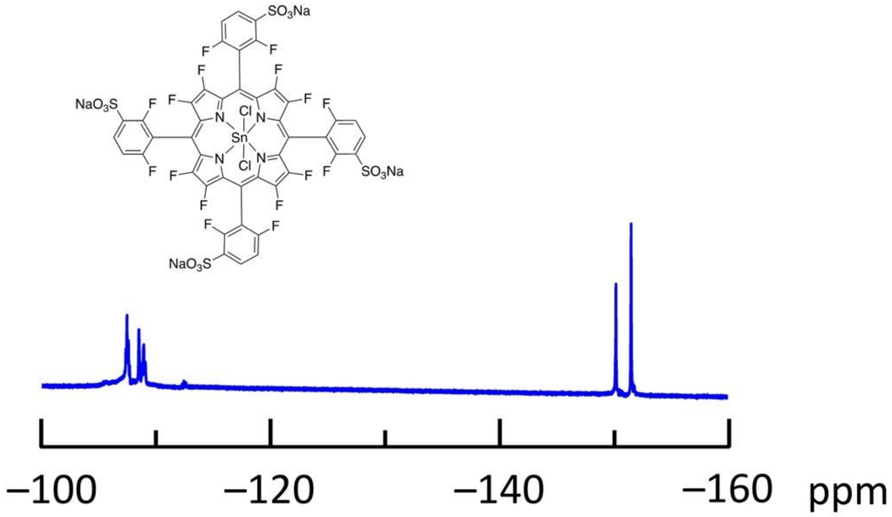

Figure AIII.6 *^{19}F NMR of $[Sn\text{-}F16P]^{4-}$ in MeOD.*

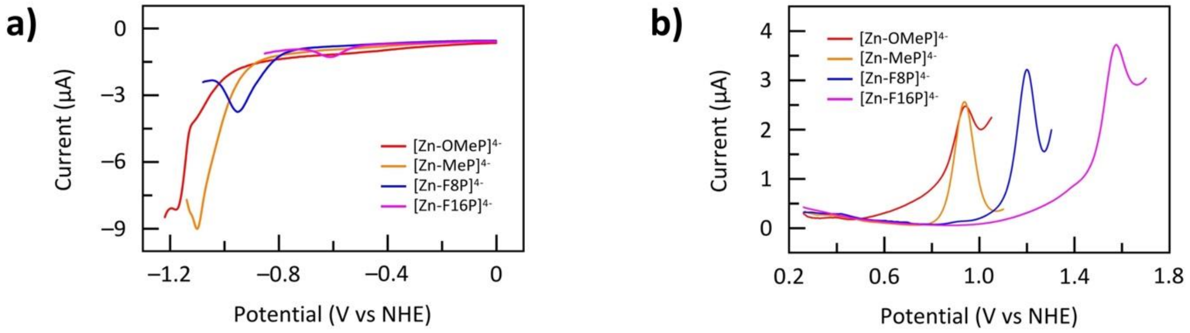

Figure AIII.7 *DPV of 1.0 mM [Zn-OMeP]$^{4-}$, [Zn-MeP]$^{4-}$, [Zn-F8P]$^{4-}$ or [Zn-F16P]$^{4-}$ in 1:1 0.1 M pH 7.0 PB/MeCN solution. Conditions: 0.07 cm^2 glassy-carbon working electrode, Pt wire auxiliary electrode, Ag/AgCl reference electrode, ±0.004 V increase potential, 0.05 V amplitude, 0.05 s pulse width, 0.0167 s sampling width, 0.5 s sample period, T = 298 K.*

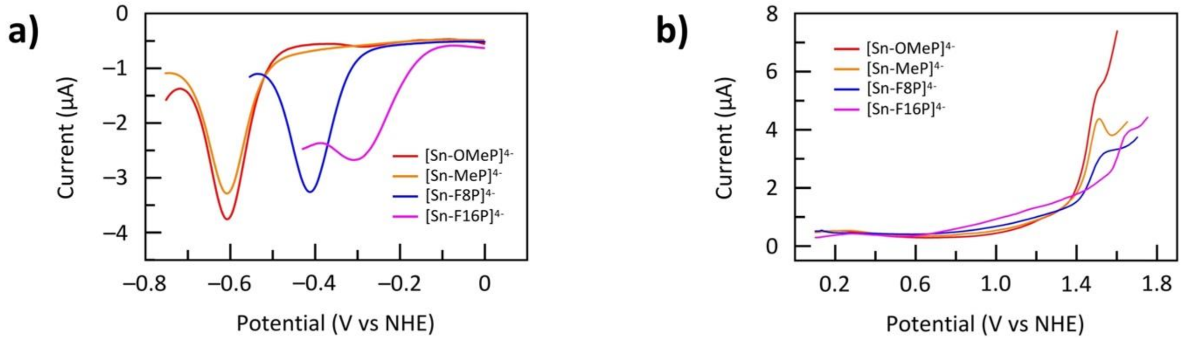

Figure AIII.8 *DPV of 1.0 mM [Sn-OMeP]$^{4-}$, [Sn-MeP]$^{4-}$, [Sn-F8P]$^{4-}$ or [Sn-F16P]$^{4-}$ in 1:1 0.1 M pH 7.0 PB/MeCN solution. Conditions: 0.07 cm^2 glassy-carbon working electrode, Pt wire auxiliary electrode, Ag/AgCl reference electrode, ±0.004 V increase potential, 0.05 V amplitude, 0.05 s pulse width, 0.0167 s sampling width, 0.5 s sample period, T = 298 K.*

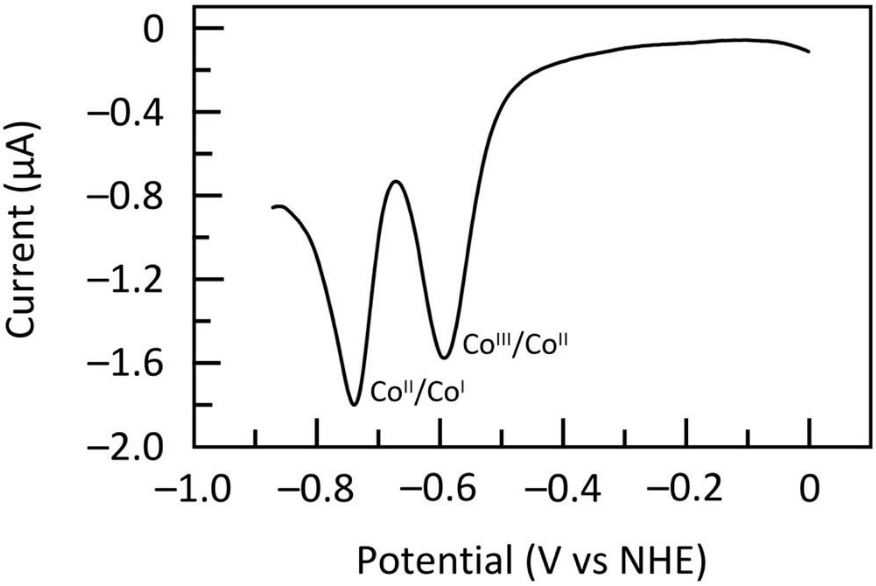

Figure AIII.9 *DPV of 0.5 mM cobaloxime in 1:1 0.1 M pH 7.0 PB/MeCN solution. Conditions: 0.07 cm*^{2} *glassy-carbon working electrode, Pt wire auxiliary electrode, Ag/AgCl reference electrode, –0.004 V increase potential, 0.05 V amplitude, 0.05 s pulse width, 0.0167 s sampling width, 0.5 s sample period, T = 298 K.*